
DATA-DRIVEN ALGEBRAIC MODELS OF THE TURBULENT PRANDTL NUMBER FOR BUOYANCY-AFFECTED FLOW NEAR A VERTICAL SURFACE

A PREPRINT

✉ **Xiaowei Xu***

Department of Mechanical Engineering
The University of Melbourne
Melbourne 3010, Victoria, Australia
xiaoweix2@student.unimelb.edu.au

✉ **Andrew S. H. Ooi**

Department of Mechanical Engineering
The University of Melbourne
Melbourne 3010, Victoria, Australia
a.ooi@unimelb.edu.au

✉ **Richard D. Sandberg**

Department of Mechanical Engineering
The University of Melbourne
Melbourne 3010, Victoria, Australia
richard.sandberg@unimelb.edu.au

April 6, 2021

ABSTRACT

The behaviour of the turbulent Prandtl number (Pr_t) for buoyancy-affected flows near a vertical surface is investigated as an extension study of Gibson & Leslie, *Int. Comm. Heat Mass Transfer*, Vol. 11, pp. 73-84 (1984). By analysing the location of mean velocity maxima in a differentially heated vertical planar channel, we identify an infinity anomaly for the eddy viscosity ν_t and the turbulent Prandtl number Pr_t , as both terms are divided by the mean velocity gradient according to the standard definition, in vertical buoyant flow. To predict the quantities of interest, e.g. the Nusselt number, a machine learning framework via symbolic regression is used with various cost functions, e.g. the mean velocity gradient, with the aid of the latest direct numerical simulation (DNS) dataset for vertical natural and mixed convection. The study has yielded two key outcomes: (i) the new machine learnt algebraic models, as the reciprocal of Pr_t , successfully handle the infinity issue for both vertical natural and mixed convection; and (ii) the proposed models with embedded coordinate frame invariance can be conveniently implemented in the Reynolds-averaged scalar equation and are proven to be robust and accurate in the current parameter space, where the Rayleigh number spans from 10^5 to 10^9 for vertical natural convection and the bulk Richardson number Ri_b is in the range of 0 and 0.1 for vertical mixed convection.

Keywords Buoyant flow · Machine learning · Turbulence modelling · Wall-bounded turbulence.

1 Introduction

Buoyancy-affected flows near a heated surface have vast engineering applications. Examples include thermal energy systems, e.g. nuclear reactor containment [Hanjalić, 2002], building ventilations [Batchelor, 1954] and geophysical flows [Wells and Worster, 2008]. The turbulent fluid flow for these applications can be numerically simulated using the Reynolds-averaged Navier-Stokes (RANS) equations. However, the model-form uncertainties induced by the buoyancy effect have been a long-standing engineering problem. One major source of uncertainty is the approximation of the turbulence closure terms, which are the Reynolds stress tensor ($-\overline{u_i u_j}$) in the momentum equation and the turbulent

*Corresponding author.

heat flux vector ($-\overline{u_i\theta}$) in the temperature equation. These terms are commonly modelled by the linear eddy viscosity model (LEVM) and standard gradient-diffusion hypothesis (SGDH). The bridge between LEVM and SGDH is the turbulence Prandtl number, which is usually defined analogous to the molecular Prandtl number $Pr \equiv \nu/\alpha$. For uni-directional flows in a channel:

$$Pr_t = \frac{\nu_t}{\alpha_t} = \frac{\overline{uv} \, d\Theta/dy}{\overline{v\theta} \, dU/dy} = \frac{\overline{uv} \, \Gamma}{\overline{v\theta} \, S}, \quad (1)$$

where ν is the molecular viscosity, α is the thermal diffusivity, ν_t is the turbulent eddy viscosity, α_t is turbulent thermal diffusivity, the mean velocity gradient $S = dU/dy$, and the mean temperature gradient $\Gamma = d\Theta/dy$.

Studies on the turbulent Prandtl number (Pr_t) via laboratory experiments, field observations and numerical simulations have a long history. Commonly, Pr_t is treated as a near unity constant (the classical Reynolds analogy, or $\nu_t \simeq \alpha_t$) for air flow as a reasonable approximation. Reviews by Reynolds [1975] and Kays [1994] for engineering flows found evidence that Pr_t deviated from unity in the near-wall region. Thus, it has been suggested that Pr_t should not be a constant but a function of the distance from the wall or the turbulent Peclet number $Pe_t = (\nu_t/\nu)Pr$. The presence of buoyancy adds complexity to the modelling of the Pr_t , because of the increasing dissimilarity between turbulent transport of momentum and heat [Li, 2019]. The existing literature has mostly paid attention to the flow near a horizontal surface, in which Pr_t is modelled according to the stability conditions caused by heat flux. Popular models include Pr_t as functions of the stability parameter $\zeta = y/L = y/(U_\tau^3/\kappa g\beta\overline{v\theta})$ [Monin and Obukhov, 1954], the gradient Richardson number $R_g = N^2/S^2$ or flux Richardson number $R_f = \mathcal{G}/\mathcal{P}$ [Gibson and Launder, 1978, Mellor and Yamada, 1982], where L is the Obukhov length, $N = \sqrt{|g\beta\Gamma|}$ is the Brunt–Väisälä frequency, and \mathcal{P} and \mathcal{G} represent shear production and buoyancy production, respectively, in turbulent kinetic energy (TKE) budgets. Recently, a more unifying framework based on the energy- and flux-budget [Zilitinkevich et al., 2013] or cospectral budget of momentum and heat fluxes [Li et al., 2015] has been introduced to analytically formulate the relationship between $Pr_t^{-1}/Pr_{t,neu}^{-1}$ and R_f [see Li, 2019, for a comprehensive review by the atmospheric community], where the subscript ‘neu’ indicates ‘neutral conditions’. The general observation is that Pr_t decreases as the flow become unstable. In contrast to the extensive study of flow near a horizontal surface, the behaviour of Pr_t near a vertical surface has rarely drawn attention. Gibson and Leslie [1984] applied a parametrized model for a vertical setup related to R_f by parametrizing second-moment transport equations that were initially employed for the ground effect near a horizontal surface [Gibson and Launder, 1978]. It is still not clear whether the aforementioned relations, developed by the atmospheric community, are applicable to the Pr_t in vertical setup; nevertheless, the budgets for second-order statistics are different. For instance, the buoyancy production $\mathcal{G} = g\beta\overline{u\theta}$ is calculated using the streamwise heat flux for a vertical configuration, whereas \mathcal{G} is based on the wall-normal heat flux for buoyant flow near a horizontal surface. Furthermore, the existence of velocity maxima ($S \rightarrow 0$) adds complexity to modelling Pr_t as it tends to infinity. Therefore, an understanding of the behaviour of Pr_t in a vertical setup warrants closer inspection.

There are several vertical configurations [Hölling and Herwig, 2005]: flow along a plate, within an enclosed cavity, along a tube or pipe [Jackson et al., 1989] and that between two infinite differentially heated vertical walls. We choose the latter configuration (see Fig. 1), a fully developed planar channel flow, because of the ideal one-dimensional averaged statistics and the availability of high-fidelity data (either direct numerical simulations (DNSs) or well-resolved large eddy simulations). Seminal works on the vertical setup include the vertical mixed convection (VMC) cases by Kasagi and Nishimura [1997] for global Reynolds number $Re_\tau = 150$ with Rayleigh number $Ra = 6.8 \times 10^5$ and the vertical natural convection (VNC) cases for Ra at $\mathcal{O}(10^6)$ [Phillips, 1996, Boudjemadi et al., 1997, Versteegh and Nieuwstadt, 1999]. Recent studies on VMC have focused on analysing the effect of near-wall large-scale structures [Fabregat et al., 2010, Wetzel and Wagner, 2019] using the same parameters. In contrast to the attention on Kasagi and Nishimura [1997], the DNS study carried out by Sutherland et al. [2015] at $Re_\tau = 395$ with several Ra cases has received rare attention from modellers. Regarding vertical natural convection, DNS studies have more recently extended the Ra to $\mathcal{O}(10^9)$ [Kiš and Herwig, 2014, Ng et al., 2015]. This paper will use the newest DNS results [Sutherland et al., 2015, Ng et al., 2015] on the buoyancy-affected vertical channel to develop suitable models.

Applying machine learning techniques based on high-fidelity data to develop physically informed turbulence models is a burgeoning field [Kutz, 2017, Duraisamy et al., 2019]. Early studies have applied an optimization method (such as field inversion and the adjoint method) or a Bayesian approach to quantify and reduce the RANS-based uncertainties by modifying turbulent closure terms, model coefficients etc. Ling et al. [2016] applied a deep neural network method to simple geometrical flows and it showed promising results. Another approach is gene expression programming (GEP) developed by Weatheritt and Sandberg [2016, 2017]. In the comparison of GEP with a deep neural network by Weatheritt et al. [2017], both approaches improved the prediction of the velocity fields for a jet-in-crossflow problem. Recently, similar training frameworks have been implemented for heat flux vector modelling [Milani et al., 2018, 2020, Sandberg et al., 2018, Weatheritt et al., 2020]. The models are developed by referring to second-order high-fidelity data in an *a priori* sense, called *frozen* training, and the *a posteriori* performance in RANS is sometimes unsatisfactory. Hence, a *CFD-driven* training approach [Zhao et al., 2020] was devised to seek better machine learnt candidate models

by directly appraising *a posteriori* performance during the training process. In this paper, we will utilize GEP with both *frozen* and *CFD-driven* training to find a proper model for Pr_t .

The primary objective of this paper is a close inspection of the behaviour of the turbulent Prandtl number for buoyancy-affected flow near a vertical surface, which has not seen sufficient attention, since the final study by Gibson and Leslie [1984]. The paper is organized as follows. In §2, the location of velocity maxima based on the latest DNS data is shown. We highlight the need for variable Pr_t in the whole domain due to the existence of an infinity anomaly for both vertical natural and mixed convection. The training framework is then presented in §3, where the detailed procedures of *frozen* and *CFD-driven* training are delineated. Here, we also present the preprocessing method on DNS-based eddy viscosity. In §4, the predictive accuracy of GEP-trained models is systematically assessed by investigating the dependency on the training dataset and cost functions. Finally, §5 concludes this paper.

2 Data source and flow features

In this section, we present the setup and the unified governing equations for VNC and VMC. Then, the DNS dataset used in the following modelling process is shown. Based on the DNS data, we discuss the behaviour of Pr_t , which encompasses several distinctive features, e.g. the existence of a singularity for the vertical buoyant flow.

2.1 Flow setup and governing equation

Fig. 1 shows a schematic with the three- and two-dimensional view of the setup used in this paper. The coordinate system (x, y, z) denotes the streamwise (opposed to gravity direction), wall-normal and spanwise directions. When using Reynolds decomposition, the flow instantaneous quantities $(\tilde{u}, \tilde{v}, \tilde{w}, \tilde{p}, \tilde{\theta})$ are expressed as the sum of the mean part (U, V, W, P, Θ) and fluctuations (u, v, w, p, θ) . The no-slip and no-penetration boundary conditions are imposed on the velocity and constant isothermal temperatures are set at the walls. Both streamwise (x) and spanwise (z) directions are periodic for velocity, pressure and temperature. This indicates $\partial/\partial y \gg \partial/\partial x, \partial/\partial z = 0, V = W = 0$. Thus, the time- and area- averaged mean profiles $U(y)$ and $\Theta(y)$ only vary along the wall-normal direction. Consequently, the Reynolds-averaged mean equations of motion can be written as:

$$0 \simeq -\frac{1}{\rho} \frac{\partial P}{\partial x} + \frac{d}{dy} \left(\nu \frac{dU}{dy} - \overline{uv} \right) + g_1 \beta (\Theta - \Theta_0), \quad (2)$$

$$0 \simeq \frac{d}{dy} \left(\alpha \frac{d\Theta}{dy} - \overline{v\theta} \right). \quad (3)$$

We treat density ρ as a constant by employing the Oberbeck–Boussinesq approximation for the density variation with temperature in the momentum equations. Furthermore, for simplicity, we prefer to use $-\overline{u_i u_j}$ instead of $-\rho \overline{u_i u_j}$ and to use $-\overline{u_i \theta}$ instead of $-\rho \overline{u_i \theta}$.

The vertical channel is controlled by two streamwise body forces: the gravity force $g_1 = -g$ and a constant mean pressure gradient $-1/\rho (\partial P/\partial x)$. The following parameters that dominate the flow, Rayleigh number Ra , bulk Reynolds number Re_b , bulk Richardson number Ri_b and Prandtl numbers $Pr \equiv \nu/\kappa$ are, respectively, defined by,

$$Ra \equiv \frac{g\beta\Delta\Theta(2h)^3}{\nu\kappa}, Re_b \equiv \frac{2hU_b}{\nu}, Ri_b \equiv \frac{Ra}{Re_b^2 Pr}, \quad (4)$$

where the half channel-width is h (full width $H = 2h$), g is the gravitational acceleration, bulk mean velocity $U_b = 1/(2h) \int_0^{2h} U(y) dy$, ν is the kinematic viscosity and κ is the thermal diffusivity. The fluid properties are assumed to be constant. The temperature difference $\Delta\Theta = \Theta_h - \Theta_c$ is defined by the scaled temperature $\Theta_h = 0.5$ on the hot plate and $\Theta_c = -0.5$ on the cold plate (see Fig. 1). It is worth noting that the mean pressure gradient in mixed convection is defined as:

$$-\frac{1}{\rho} \frac{\partial P}{\partial x} = \frac{U_{\tau,h}^2 + U_{\tau,c}^2}{2h}, \quad (5)$$

where the friction velocities are $U_{\tau,h} = \sqrt{\nu dU/dy|_{w,h}}$ at the hot wall and $U_{\tau,c} = \sqrt{\nu dU/dy|_{w,c}}$ at the cold wall. In addition, the global mean friction velocity is defined by the arithmetic mean of the one at each wall, that is, $U_\tau = (U_{\tau,h} + U_{\tau,c})/2$. For forced convection, $U_\tau = U_{\tau,h} = U_{\tau,c}$, and $(-1/\rho) \partial P/\partial x = U_\tau^2/h$. Lastly, the Nusselt number, the dimensionless heat transfer rate, is quantified as $Nu \equiv f_w(2h)/(\Delta\Theta\kappa)$ where $f_w \equiv \kappa |d\Theta/dy|_w$, $|d\Theta/dy|_w$ is the mean temperature gradient at the hot and cold walls.

There are two limit states for the current setup, namely, pure buoyancy-driven flow (referred to as natural or free convection) and pure shear-driven flow (referred to as forced convection), which can be quantified by the bulk Richardson

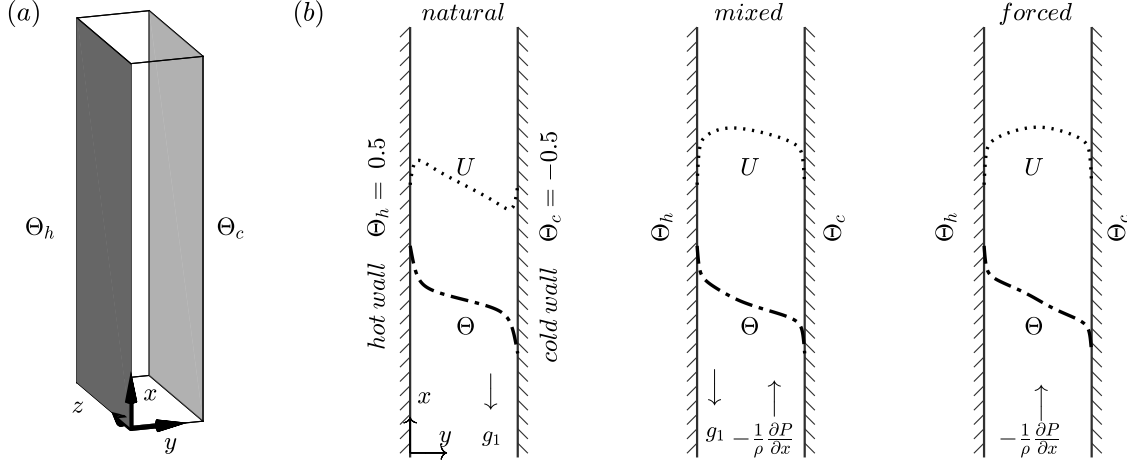


Figure 1: A schematic diagram of the setup of an infinite vertical channel, (a) three-dimensional view of domain used for DNS; (b) two-dimensional view with the shape of mean velocity $U(y)$ and temperature $\Theta(y)$ profiles, from left to right: natural convection (solely driven by gravitation force g_1), mixed convection (driven by a combination of g_1 and a constant mean pressure gradient $-\frac{1}{\rho} \frac{\partial P}{\partial x}$) and forced convection (solely driven by $-\frac{1}{\rho} \frac{\partial P}{\partial x}$).

number Ri_b . Increasing Ri_b means adding a buoyancy effect; if $Ri_b = 0$, it means $g = 0$, and the flow is the canonical channel flow (forced convection), while as $Ri_b \rightarrow \infty$ (namely, $U_b = 0$), the flow is purely buoyancy-driven (natural convection). Fig. 1 (b) is a two-dimensional view of the vertical channel, from left to right: natural, mixed and forced convection. In each panel, the mean velocity $U(y)$ and mean temperature $\Theta(y)$ are plotted to show the velocity maxima for the three scenarios.

This paper employs different nondimensionalizations for natural, mixed or forced convection due to the distinctive features of shear-dominant and buoyancy-dominant flows. For natural convection, we choose the traditional full width H as the length scale and H/U_f (where the velocity scale is the free fall velocity $U_f = \sqrt{g\beta\Delta\Theta H}$ [Ng et al., 2015]) as time scale. For forced and mixed convection, the length scale is the half channel-width h , and the time scale is h/U_τ . Note that the mechanical turbulent dissipation rate ε is normalized by U_f^3/H for VNC and U_τ^4/ν for VMC.

2.2 DNS dataset

In this study, 14 cases of the DNS dataset are used (see Table 1), which were carried out by Ng et al. [2015] (Set A, Case 1 ~ 7) for VNC and Sutherland et al. [2015] (Set B, Case 8 ~ 14) for VMC with $Pr = 0.709$ (for air flow). The cases cover the range of Reynolds and Rayleigh numbers $0 \leq Re_b \leq 1.471 \times 10^4$, $10^5 \leq Ra \leq 10^9$. We adopt the label Rax_Rey [Pirozzoli et al., 2017] at $Ra = 10^x$, $Re_b = 10^y$. For instance, the flow case 11, $Ra6.5_Re4.2$, denotes $Ra = 3.6 \times 10^6 = 10^{6.5}$ and $Re_b = 1.471 \times 10^4 = 10^{4.2}$. Besides, $Ra = 0$ corresponding to pure Poiseuille flow (forced convection), and $Re_b = 0$ corresponding to VNC. Table 1 also provides a shorthand label, for instance, $Ra80$ for the natural convection case at $Ra = 1.0 \times 10^8$ and $Ri50$ for the mixed convection case at $Ri_b = 0.050$.

2.3 The behaviour of the turbulent Prandtl number in global coordinates

For the one-dimensional mean flow field, the governing equations only include the two components of the Reynolds stress tensor and heat flux vector, which are the Reynolds shear stress (\overline{uv}) and the wall-normal heat flux ($\overline{v\theta}$) for a planar channel flow. We adopted the well-established linear gradient LEVM and SGDH models as the starting point, which are, respectively,

$$-\overline{uv} = \nu_t \frac{dU}{dy}, \quad (6)$$

$$-\overline{v\theta} = \alpha_t \frac{d\Theta}{dy} = \frac{\nu_t}{Pr_t} \frac{d\Theta}{dy}. \quad (7)$$

First and foremost, it is essential to discuss the signature of the mean velocity gradient dU/dy and mean temperature gradient $d\Theta/dy$, \overline{uv} , $\overline{v\theta}$ in global coordinates. Gibson and Leslie [1984] listed the major features along the vertical

Case	Label	Flow case	Ri_b	Ra	Re_b	Nu	Flow type	Purposes	
A	1	Ra50	Ra5_Re0	∞	1.0×10^5	0	57.53	natural	testing
	2	Ra57	Ra5.7_Re0	∞	5.4×10^5	0	29.18	natural	training & testing
	3	Ra63	Ra6.3_Re0	∞	2.0×10^6	0	16.64	natural	testing
	4	Ra66	Ra6.6_Re0	∞	5.0×10^6	0	10.82	natural	testing
	5	Ra73	Ra7.3_Re0	∞	2.0×10^7	0	8.15	natural	training & testing
	6	Ra80	Ra8_Re0	∞	1.0×10^8	0	5.37	natural	testing
	7	Ra90	Ra9_Re0	∞	1.0×10^9	0	3.04	natural	training & testing
B	8	Ri00	Ra0_Re4.1	0	0	13846	12.75	forced	training & testing
	9	Ri13	Ra6.3_Re4.2	0.013	1.9×10^6	14239	12.79	mixed	testing
	10	Ri18	Ra6.3_Re4.1	0.018	2.2×10^6	12963	12.32	mixed	testing
	11	Ri23	Ra6.5_Re4.2	0.023	3.6×10^6	14710	13.57	mixed	testing
	12	Ri35	Ra6.6_Re4.1	0.035	4.0×10^6	12696	12.86	mixed	testing
	13	Ri50	Ra6.9_Re4.2	0.050	8.3×10^6	15232	14.88	mixed	training & testing
	14	Ri94	Ra6.9_Re4.2	0.094	9.3×10^6	11825	13.54	mixed	training & testing

Table 1: DNS dataset of flow cases, $Re_b = 2hU_b/\nu$ is the bulk Reynolds number, $Ri_b = 2\beta g\Delta\theta h/U_b^2$ is the bulk Richardson number, $Ra_y = \beta g\Delta\theta(2h)^3/(\alpha\nu)$ is the Rayleigh number, $Nu = (2h/\Delta\theta)|d\theta/dy|_w$ is the Nusselt number. Set A, Case 1 ~ 7, Ng et al. [2015]; Set B, Case 9 ~ 14, Sutherland et al. [2015]; more details are showed in Appendix A. In the *Purposes* column, the training and testing datasets are showed, in which the *training* represents the cases used to train a machine learnt model, and *testing* represents the cases used for cross-validation.

surface; they are mostly true only if the flow is in or near the buoyancy-driven/buoyancy-dominated regime. From DNS studies [see Versteegh and Nieuwstadt, 1999, Fig. 2 (c)] on the vertical natural convection, the adapted version is,

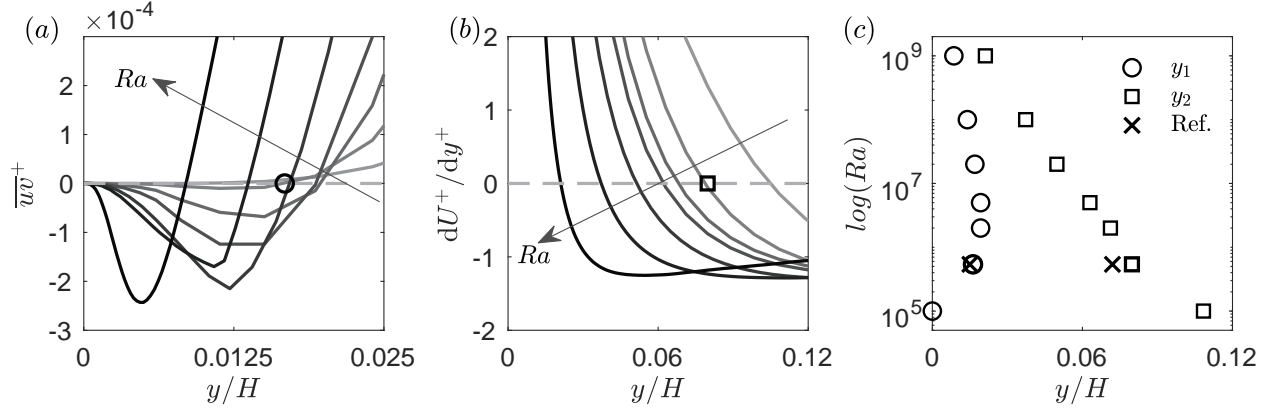


Figure 2: Division of region in VNC: (a), y_1 is the zero point of \overline{uw} , and (b), y_2 is the zero point of dU/dy in the region between the hot wall ($y/H = 0$) and the centreline ($y/H = 0.5$). The greyscale from light to dark that varies with the increase in Ra from 10^5 to 10^9 is based on Ng et al. [2015]; see Table 1 for details on DNS cases. The y_1 and y_2 values for $Ra = 5.4 \times 10^5$ are explicitly shown in (a) and (b). (c), the variation in y_1 and y_2 with the change in Ra , where the *Ref.* \times is a verification case in Versteegh and Nieuwstadt [1999] at $Ra = 5.4 \times 10^5$.

- (i) The temperature gradient ($d\theta/dy$) is negative everywhere, and the wall-normal heat flux ($\overline{v\theta}$) is positive everywhere;
- (ii) The Reynolds shear stress (\overline{uw}) is negative for small y_w and positive for large y_w , where y_w is the nearest distance from the wall (or wall distance).
- (iii) The turbulent Prandtl number Pr_t has singularities and a negative region in the vicinity of the wall.

For a clear discussion regarding the division of the regions, we define y_1 as the zero point of \overline{uw} and y_2 as the zero point of dU/dy in the region of the hot wall ($y = 0$) to the centerline ($y = h$). Fig. 2 (a) and (b) shows the exact position of y_1 and y_2 , which results in the sign of key quantities (see Table 2). For the whole domain in global coordinates, a

laminar sublayer exists within $0 < y_w < y_1$ and a turbulent layer within $y_2 < y_w < h$. The $y_1 < y_w < y_2$ region is actually the bridge between these two distinctive regions, which can be called the adjustment region [Wells and Worster, 2008]. Fig. 2 (c) shows that the adjustment region shrinks with the increase in Ra and might diminish when $Ra \rightarrow \infty$ [Hölling and Herwig, 2005]. Meanwhile, Ng et al. [2017] suggest that the thermal and viscous boundary layers undergo a transition from a classical laminar-like state to the ultimate shear-dominated state from moderate to high Ra . Therefore, given the diminishing of the adjustment region and the transition of the laminar sublayer, the whole domain could be turbulent in the ultimate state. From the point of view of the modeller, the adjustment region is the area where the LEVM [Versteegh and Nieuwstadt, 1999] is not valid near both walls. In other words, the infinity issue occurs in both Pr_t (see Eq. 1 and Fig. 3 (b)) and $\nu_t^{dns} = -\overline{wv}/(dU/dy)$ (see Fig. 3(c)) in global coordinates. Collectively, the infinity issue at Ra from 10^5 to 10^9 is a challenging question for symbolic regression and model generality in this study.

region	dU/dy	$d\Theta/dy$	\overline{wv}	$\overline{v\theta}$	ν_t	Pr_t
$0 < y_w < y_1$	+	-	-	+	+	+
$y_1 < y_w < y_2$	+	-	+	+	-	-
$y_2 < y_w < h$	-	-	+	+	+	+

Table 2: The sign of quantities along wall-normal direction until the centreline in global coordinates for VNC.

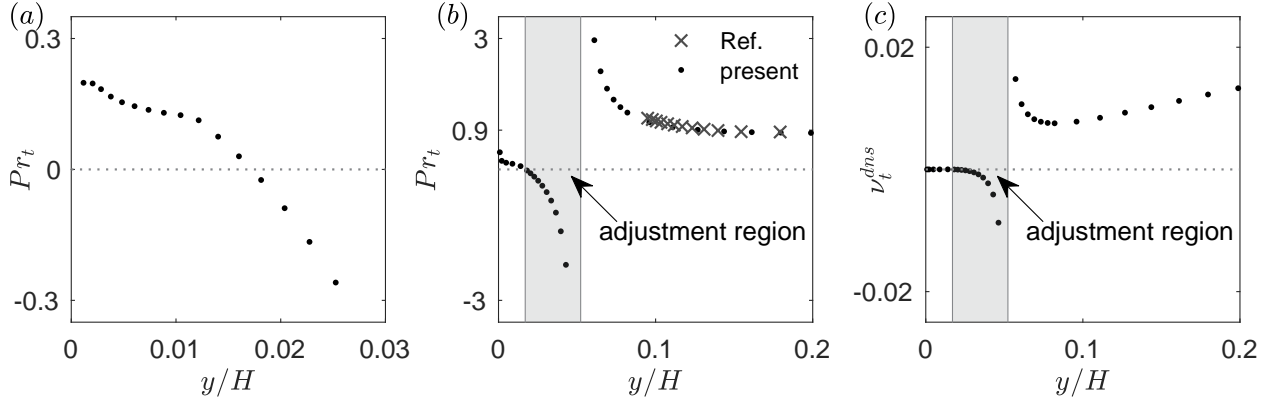


Figure 3: The distribution of turbulent Prandtl number (Pr_t) and eddy viscosity ν_t^{dns} at $Ra = 5.0 \times 10^6$ for VNC, where (a), Pr_t in the near-wall positive region; (b), Pr_t in global coordinates, where the present data are validated against Dol et al. [1999] (\times); (c), ν_t^{dns} in global coordinates. The grey patch depicts the adjustment region between y_1 and y_2 .

For vertical mixed convection, Fig. 4 (a) and (b) shows that when $Ri_b = 0$ (forced convection), the profiles of \overline{wv} and dU/dy have symmetry and the zero points stay at the centreline ($y/h = 1$). With an increase in Ri_b , both profiles gradually shift to the hotter wall side. Fig. 4 (c) illustrates the zero points y_1 and y_2 are almost at the same position until $Ri_b \simeq 0.10$. It is still not clear whether y_1 and y_2 are mathematically the same. Nevertheless, the mismatch between y_1 and y_2 is negligible. Thus, the LEVM is approximately valid in the whole domain for $0 \leq Ri_b < 0.10$. The resulting adjustment region is illustrated in Fig. 5 for Pr_t and Fig. 8 for ν_t^{dns} . It is worth noting that Pr_t is larger than unity within the viscous sublayer ($y^+ < 10$), which is quite different with respect to the buoyant horizontal channel [Pirozzoli et al., 2017]. Meanwhile, the discrepancy of Pr_t between the hotter and colder wall at the same y^+ becomes larger with the increase in Ri_b . To summarize, the most distinctive feature is the break of symmetry for the mean and second moment statistics for VMC compared with the pure shear or buoyancy-driven vertical flow and horizontal channel [Garcia-Villalba and del Alamo, 2011, Pirozzoli et al., 2017]. Moreover, The asymmetry causes several modelling issues, such as the implementation of wall distance y_w or y^+ for the low- Re approach.

3 Modelling Methodologies

In this section, we present the modelling framework via GEP with *frozen* and *CFD-driven* training. Then, the RANS-based approximation method for recovering DNS-based input quantities is introduced.

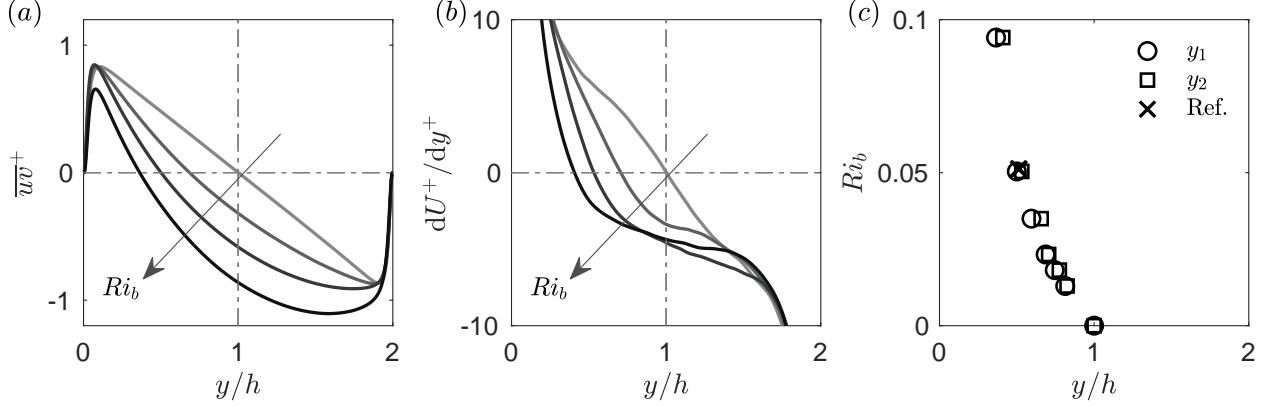


Figure 4: Position of the zero point in VMC: (a) y_1 is the zero point of \overline{wv} , and (b) y_2 is the zero point of dU/dy in the whole domain (hot wall $y/h = 0$, cold wall $y/h = 2$). The greyscale from light to heavy that varies with the increase in Ri_b , which is 0, 0.023, 0.050, 0.094, is based on Sutherland et al. [2015]; see Table 1 for detailed DNS cases. (c) is the variation in y_1 and y_2 with the change in Ri_b , where the Ref. \times is a verification case in Kasagi and Nishimura [1997] at $Ri_b = 0.051$ (according to Figure 10, for the stress balance, Case 3f, $Re_\tau = 150$ and $Ra = 6.8 \times 10^5$).

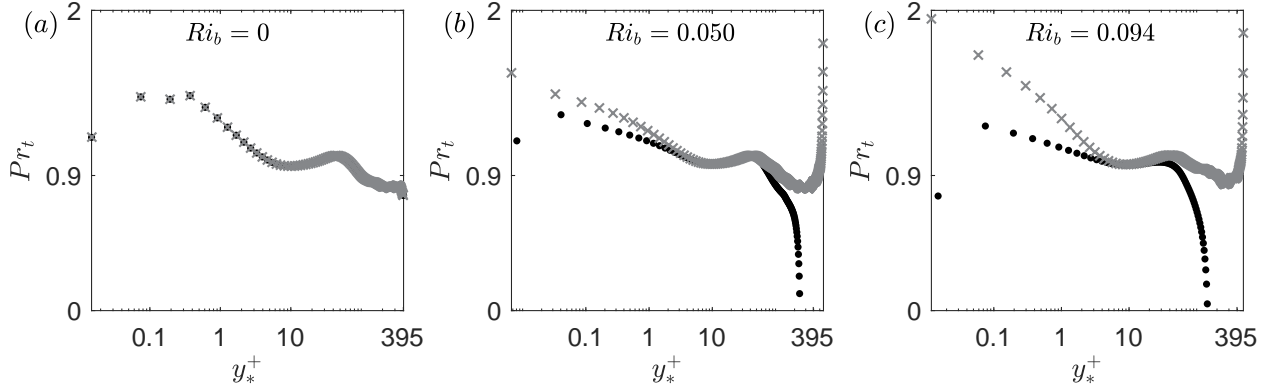


Figure 5: Turbulent Prandtl number (Pr_t) for VMC, where (a) $Ri_b = 0$; (b) $Ri_b = 0.050$; (c) $Ri_b = 0.094$, where \bullet indicates being near the hotter wall; \times indicates being near the colder wall. The wall unit, $y_*^+ = y_h^+ = y_w U_{\tau,h}/\nu$ at the hotter wall and $y_*^+ = y_c^+ = y_w U_{\tau,c}/\nu$ at the colder wall.

3.1 Training framework

For modelling scalar flux, the goal is to find a mathematical representation of $\overline{u_i \theta}$. Based on dimensional arguments, Shih and Lumley [1993] showed that $\overline{u_i \theta} = f(U_{i,j}, \Theta_{,i}, k, \varepsilon, \overline{\theta^2}, \varepsilon_\theta)$, where $\overline{\theta^2}$ denotes the temperature variance and ε_θ denotes the dissipation rate in a thermal field. This can be further simplified by assuming a sole time scale ($\overline{\theta^2}/\varepsilon_\theta \simeq k/\varepsilon$), which means that the thermal to mechanical time ratio, $\mathcal{R} = \overline{\theta^2}\varepsilon/(k\varepsilon_\theta)$ is treated as a near unity constant [Dol et al., 1999]. Hence, we obtain $\overline{u_i \theta} = f(U_{i,j}, \Theta_{,i}, k, \varepsilon)$. In light of Galilean invariance and nondimensionalization, a dimensionless velocity invariant I and a dimensionless temperature invariant J [Weatheritt et al., 2020] are used to construct the target scalar flux models,

$$I = \left(c_\mu \frac{k}{\varepsilon}\right)^2 S_{ij} S_{ji} = \frac{1}{2} \left(c_\mu \frac{k}{\varepsilon} \frac{dU}{dy}\right)^2, \quad (8)$$

$$J = \left(c_\mu \frac{k^{1.5}}{\varepsilon} \frac{d\Theta}{dy}\right)^2, \quad (9)$$

where the mean strain rate tensor $S_{ij} = \frac{1}{2}(U_{i,j} + U_{j,i})$, $c_\mu = 0.09$. We adopt a variable turbulent Prandtl number Pr_t with the reciprocal form $f(I, J) = Pr_t^{-1}$ and calculate the turbulent thermal diffusivity α_t ,

$$\alpha_t = \frac{\nu_t}{Pr_t} = f(I, J)\nu_t. \quad (10)$$

Note that the commonly used SGDH adopts a constant turbulent Prandtl number $Pr_t = 0.80 \sim 1.10$ (equivalent to $1/f(I, J)$ in the models proposed here) for air.

3.1.1 Frozen training

The machine learning procedure employs an in-house symbolic regression tool based on GEP, which was initially developed and tested for Reynolds stress closures by Weatheritt and Sandberg [2016] and was recently used in scalar flux modelling [Weatheritt et al., 2020]. In general, we treat the wall-normal heat flux $\overline{v\theta}$ as a target term and regress by the constraint of cost function $J(\overline{v\theta})$; see Eq.11, where a square root error is calculated along the wall-normal direction of $\varphi = \overline{v\theta}$, with superscript *dns* representing data from direct numerical simulation, and *gcp* the value from simulation by GEP models).

$$J(\varphi) = \int_{dy} (\varphi^{dns} - \varphi^{gcp})^2 dy \quad (11)$$

This approach is called *frozen* training [Zhao et al., 2020] as we are trying to optimize a closure against a fixed high-fidelity database. The detailed procedure can be found in Algorithm 1. Moreover, before running GEP, there are two preprocessing steps. One possible issue is the lack of a DNS-based dissipation rate ε suitable for the modelling. We overcome this issue by solving the transport equation of ε (see Eq. 12) with $c_{1\varepsilon} = 1.44$, $c_{2\varepsilon} = 1.92$, $\sigma_\varepsilon = 1.3$, where all the other quantities, such as $\overline{v\theta}$, U , Θ , k , are extracted from DNS

$$-\frac{\varepsilon}{k} [c_{1\varepsilon}(\mathcal{P} + \mathcal{G}) - c_{2\varepsilon}\varepsilon] = \frac{d}{dy} \left[\left(\nu + \frac{\nu_t}{\sigma_\varepsilon} \right) \frac{d\varepsilon}{dy} \right] \quad (12)$$

and $\mathcal{P} = -\overline{uv} dU/dy$, $\mathcal{G} = g\beta\overline{u\theta}$. Another step is the way to approximate ν_t (the infinity issue discussed in §2.3), which is delineated in §3.2.

Algorithm 1: frozen training

- 1 Get $\overline{v\theta}$, U , Θ , k from DNS data,
 - 2 **if** do not have suitable DNS-based ε **then**
 - 3 | Solve transport equation of ε (Eq. 12) with DNS-based $\overline{v\theta}$, U , Θ , k as input
 - 4 **end**
 - 5 Calculate positive smoothed $\nu_t^{mod} = f_\mu c_\mu k^2 / \varepsilon$ for VMC, Eq. 15 for VNC
 - 6 **for** each generation step $i = 1, 2, \dots, N$ **do**
 - 7 | randomly generate population in the environment
 - 8 | **for** each population step $j = 1, 2, \dots, M$ **do**
 - 9 | | genetic evolution to find the best candidate models based on the minimum fitness $J(\overline{v\theta})$ for the i^{th} generation
 - 10 | **end**
 - 11 **end**
 - 12 Solve RANS scalar equation with new model to obtain Θ , Nu
-

3.1.2 CFD-driven training

The resulting data-driven models via *frozen* training can improve the performance of $\overline{v\theta}$, but sometimes the improvement fails to be shown in the mean flow field Θ and Nusselt number Nu . To find better turbulent heat flux models, we implement a loop algorithm that integrates GEP and a RANS solver, referred to as *CFD-driven* training [Zhao et al., 2020] (see Algorithm 2). The major modification compared with *frozen* training is solving the RANS scalar equation for each candidate model and then obtaining the RANS-based Θ , $d\Theta/dy$ and Nu to calculate the cost function (see Eq.13) in terms of quantities of interest. For example, the cost function can be the error of mean temperature $J(\Theta)$ (Eq.11, where $\varphi = \Theta$). We can also use the absolute error of Nu ($J(Nu)$ in Eq.13a), or the combination of errors, such as $J(cNu)$ in Eq. 13b and $J(cdc)$ in Eq. 13c.

Algorithm 2: CFD-driven training

```

1 Get  $\overline{v\theta}, U, \Theta, k$  from DNS data, calculate  $\varepsilon, \nu_t$  (same as frozen training)
2 for each generation step  $i = 1, 2, \dots, N$  do
3   randomly generate population in the environment
4   for each population step  $j = 1, 2, \dots, M$  do
5     feed  $f(I, J)$  into RANS scalar equation for  $\alpha_t$ 
6     solve the RANS scalar equation for each candidate model for the  $i^{th}$  generation and obtain  $\Theta, Nu$ 
7     find best candidate models constrained by customized cost  $J(\varphi)$  based on  $\Theta$  or  $d\Theta/dy$  for the  $i^{th}$ 
      generation
8   end
9 end

```

$$J(Nu) = \frac{|Nu^{dns} - Nu^{gep}|}{Nu^{dns}} \times 100\%, \quad (13a)$$

$$J(cNu) = J(\Theta) + \lambda J(Nu), \quad (13b)$$

$$J(cdc) = J(\Theta) + \lambda J(d\Theta/dy). \quad (13c)$$

3.2 Data preparation of DNS-based input quantities

In §2.3, a close inspection of the flow features at different regions allows us to identify some issues with the linear gradient-based assumption and the validity of LEVM, especially the near-wall region for VNC. In practice, as the mean velocity gradient $dU/dy \rightarrow 0$ at y_2 , that is, ν_t^{dns} could be a non-physical value in the vicinity of the wall region as it tends to $\nu_t^{dns} \rightarrow \pm\infty$

$$\nu_t^{dns} = \frac{-\overline{wv}}{dU/dy} \quad (14)$$

Here, by assuming a smooth and positive ν_t [Xu et al., 1998], for VNC, we devise a limiter function (see Eq. 15) under the condition γ , where γ is $|dU/dy| \leq 1.2 \cap y_w/H < 0.12$ to remove the singularity for the region of the infinity anomaly. The empirical constants in Eq.15 are obtained according to DNS data, which can be seen in Fig. 2 (b). More specifically, $y_w/H < 0.12$ gives the upper bound of the near-wall region for the smoothing operation and $|dU/dy| \leq 1.2$ provides a good estimate for the infinity anomaly region for all Ra from 10^5 to 10^9 . Fig. 6 illustrates the performance of Eq. 15 at $Ra = 5.4 \times 10^5$ and $Ra = 1.0 \times 10^8$. It is clear that this limiter function can successfully remove the singularity and smoothly link the near-wall laminar and the bulk turbulent regions.

$$\nu_t^{mod} = \begin{cases} \frac{\frac{|\overline{wv}|}{|dU/dy|}}{\max(|dU/dy|, 1.2)} & \text{if condition } \gamma \\ \frac{|\overline{wv}|}{|dU/dy|} & \text{else} \end{cases} \quad (15)$$

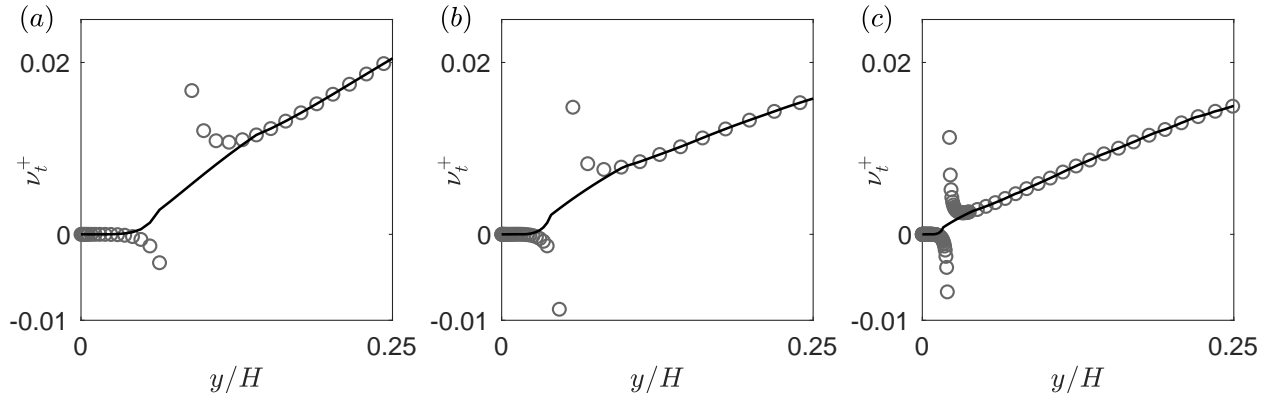


Figure 6: The smoothed turbulent eddy viscosity $\nu_t^+ = \nu_t/(HU_f)$ for VNC: (a), $Ra = 5.4 \times 10^5$; (b), $Ra = 2.0 \times 10^7$; (c), $Ra = 1.0 \times 10^9$, where \circ indicates DNS-based ν_t^{dns} (see Eq. 14); — indicates ν_t^{mod} based on Eq. 15.

A treatment of the eddy viscosity is also needed in VMC. Unlike the anti-symmetric mean profile in VNC, the asymmetry increases the complexity of identifying the position of y_2 (see Fig. 4) at different Ra_b . Hence, we use a

damping function f_μ based on the low Reynolds number modelling approach instead of the limiter function in VNC. The damping function f_μ [Myong and Kasagi, 1990] is

$$f_\mu = 1 + 3.45/\sqrt{Re_t} [1 - \exp(-y^+/70)]^2, \quad (16)$$

where local Reynolds number $Re_t = k^2/(\nu\varepsilon)$, the viscous length scale $y^+ = y_w U_\tau/\nu$. Eq. 16 is compared to DNS-based f_μ^{dns} for the $Ri00$ case (forced convection) in Fig. 7 (a), in which we can see that the near-wall (within $y^+ < 10$) prediction is fairly good. Hence, $\nu_t^{mod} = f_\mu c_\mu k^2/\varepsilon$ can be estimated quite well (Fig. 7). The damping

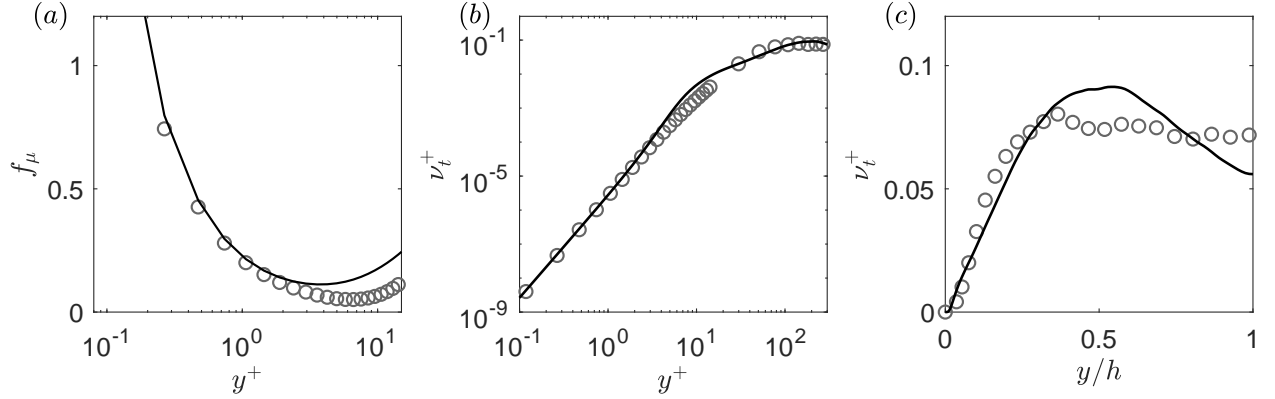


Figure 7: The turbulent eddy viscosity $\nu_t^+ = \nu_t/U_\tau h$ for forced convection, (a) distribution of the damping function, Eq. 16, —; $f_\mu^{dns} = \frac{1}{c_\mu} \frac{-\overline{uv}}{dU/dy} \frac{\varepsilon}{k^2}$, \circ . The approximated $\nu_t^{mod} = f_\mu c_\mu k^2/\varepsilon$ is —; DNS-based ν_t^{dns} is \circ in wall units in (b) and in global coordinates in (c).

function is further tested in the VMC case. Fig. 8 shows that f_μ finds the best approximation with respect to several other damping functions [see Rodi and Mansour, 1993, for a review on the low Reynolds number modelling approach]. Note that the friction velocity at the hot and cold wall is different. Hence, Figs. 8 (b) and (c) give the comparison at both walls in wall units.

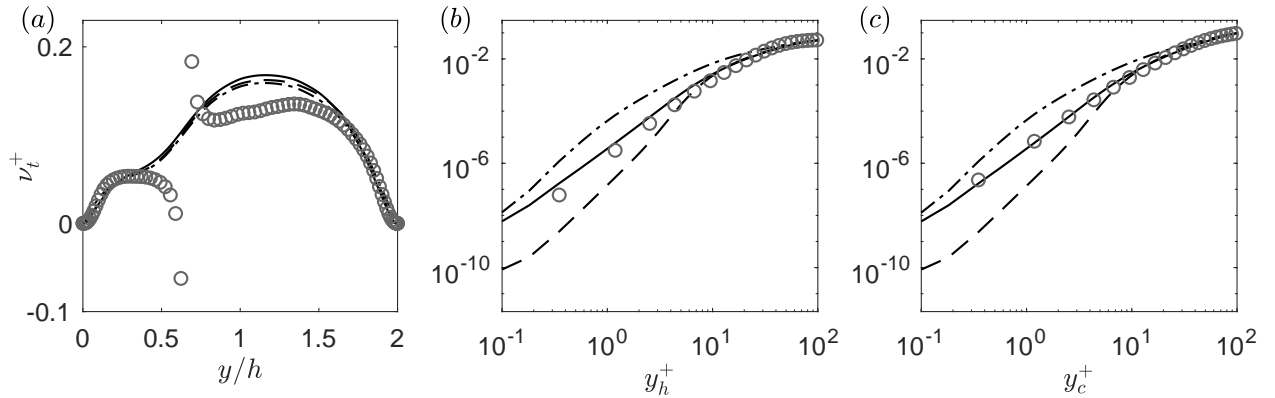


Figure 8: The turbulent eddy viscosity $\nu_t^+ = \nu_t/U_\tau h$ for VMC at $Ri_b = 0.050$, approximated by Eq. 16, where $\nu_t^{mod} = f_\mu c_\mu k^2/\varepsilon$ is indicated by — and DNS-based ν_t^{dns} is indicated by \circ . The other damping functions are the standard $k-\varepsilon$ model where $f_\mu = 1$, - - -; and the Lam-Bremhorst model where $f_\mu = [1 - \exp(-0.0165\sqrt{k}y_w/\nu)]^2 (1 + 20.5/Re_t)$, - - - . (a) in global coordinates; (b) in viscous wall units at the hotter wall $y_h^+ = y_w U_{\tau,h}/\nu$; (c) in viscous wall units at the colder wall $y_c^+ = y_w U_{\tau,c}/\nu$.

4 Results

In this section, the machine learnt models are first presented. Then, we appraise the performance of the models resulting from various training datasets and approaches by comparisons with the DNS database. Last, an *a priori* test on the turbulent Prandtl number and an *a posteriori* assessment for quantities of interest are shown.

4.1 Machine learnt models

The GEP training approaches (Algorithms 1 and 2) are applied the dataset in Table 1. Here, we delineate the detailed information of a machine learning case for VNC at $Ra = 2.0 \times 10^7$. Fig. 9 shows the normalized error metric (in this case, $J(\bar{v}\theta)$ via *frozen* training) in the training process. The population mean error dramatically decays until the 100th generation during the GEP evolution process. After the 100th generation, the population mean error fluctuates around a fixed value, and the population minimum stays at a relatively small value. Thus, the 100th generation candidate model is chosen, which is

$$f(I, J) = \underbrace{1.116}_{const.} + \underbrace{(0.205I - 12J)}_{invariants}. \quad (17)$$

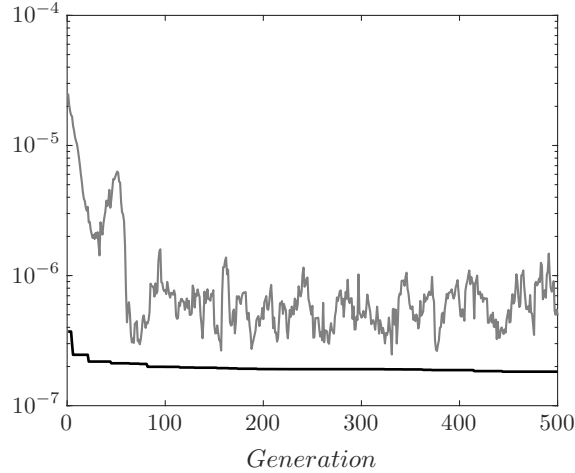


Figure 9: Evolutionary algorithm performance: —, (grey solid line) the population mean; —, (black solid line) the population minimum.

For *CFD-driven* machine learning, the computer costs are augmented by solving a RANS scalar equation for the candidate models in each generation. For a personal computer (4 cores, Intel core i7-7500U), the training procedure, involving around 2×10^4 RANS calculations (100 generations and 200 population size), takes approximately 27 hours. (Each RANS calculation takes around 20 seconds on one core to converge with the baseline results as initial condition). Besides, the resulting models are more compact than the *frozen* approach, as indicated by Zhao et al. [2020], and have the form of $f(I, J) = 0.969 + 2J$, for instance, in case of *ncgrad*.

For RANS model development in turbulent wall-bounded flow, a long-standing struggle is to satisfy the wall asymptotic behaviour. Due to the no-slip condition for velocity terms, the isothermal condition at both walls, and the continuity equation, we can derive that $v \propto \mathcal{O}(y^2)$, $u, w, \theta \propto \mathcal{O}(y^1)$, where $\propto \mathcal{O}(y^n)$ indicates a quantity is proportional to the n th order of the wall-normal coordinate. Then, it directly suggests $\bar{v}\theta \propto \mathcal{O}(y^3)$, $\frac{d\theta}{dy} \propto \mathcal{O}(y^0)$. For our model target, $\nu_t \propto \mathcal{O}(y^3)$, $\alpha_t \propto \mathcal{O}(y^3)$, $Pr_t \propto \mathcal{O}(y^0)$; hence, $f(I, J) \propto \mathcal{O}(y^0)$. In Eq. 17, Table 3 and Table 4, the GEP resulting models always have a constant term and thus satisfy $\mathcal{O}(y^0)$. The other terms consist of invariants $I \propto \mathcal{O}(y^4)$ and $J \propto \mathcal{O}(y^6)$, which means the I and J terms do not affect the near-wall asymptotic behaviour. Overall, comparing $f(I, J) \propto \mathcal{O}(y^0)$, it indicates that the GEP approach can ensure the correct wall-limiting behaviour. All the *a priori* and *a posteriori* assessments for these models are described in the following text.

4.2 Sensitivity study on training datasets and training approaches

Following the same numerical treatment, we obtain a series of resulting GEP models via *frozen* and *CFD-driven* training. Table 3 lists the models for the VNC cases, which are trained on $Ra = 2.0 \times 10^7$. For the VMC cases, Table 4 shows

Label	Training approach	Cost function	Heat flux models $f(I, J)$
<i>base</i>	-	-	1.111 ($Pr_t = 0.90$)
<i>ncflux</i>	frozen	$J(\overline{v\theta})$	$1.116 + 0.205I - 12J$
<i>ncmean</i>	CFD-driven	$J(\Theta)$	$1.195 - I + J$
<i>ncnu</i>	CFD-driven	$J(Nu)$	$1.031 - I$
<i>ncgrad</i>	CFD-driven	$J(d\Theta/dy)$	$0.969 + 2J$

Table 3: GEP models for VNC based on $Ra = 2.0 \times 10^7$ via GEP in form of $f(I, J)$.

Label	Training approach	Cost function	Heat flux models $f(I, J)$
<i>base</i>	-	-	1.111 ($Pr_t = 0.90$)
<i>mcflux</i>	frozen	$J(\overline{v\theta})$	$1.057 - 0.565I - 0.188J$
<i>mcmean</i>	CFD-driven	$J(\Theta)$	$1.000 + 0.861I(-0.215 + I - 0.5J)$
<i>mcgrad</i>	CFD-driven	$J(d\Theta/dy)$	$1.099 + I(-1.180 - 0.900J)$
<i>mccnu</i>	CFD-driven	$J(\Theta) + \lambda_1 J(Nu)$	$0.970 - 0.305I^2$
<i>mccdc</i>	CFD-driven	$J(\Theta) + \lambda_2 J(d\Theta/dy)$	$1.090 - I$

Table 4: GEP models for VMC based on $Ri_b = 0.050$ via GEP in the form of $f(I, J)$, The combination factor λ is used to ensure the error metric at the same magnitude, where $\lambda_1 = 0.1$, $\lambda_2 = 20$.

the models that are trained on $Ri_b = 0.05$. In this section, the dependence on the training datasets and cost functions are presented to seek the best model in an *a posteriori* sense.

4.2.1 Dependence on training datasets

Since the data-driven approach can depend on the training case, it is essential to cross-validate each model. We adopt a holdout training and testing approach, where a Ra or Ri_b case are selected to train a model and other cases are used to test the performance of this model. The dependence on training datasets (or cases) is studied for both VNC and VMC. Fig. 10 and Fig. 11 lay out the error of Nu and Θ , respectively, with comparison of the *a posteriori* performance across Ra for VNC. Note that we omit the other GEP models for cross-validation.

Fig. 10(a) presents the correlation map depicting the performance of trained models for Nu in an *a posteriori* sense via the frozen approach with cost function $J(\overline{v\theta})$. The legend is scaled by the absolute percentage error $J(Nu)$ of the baseline model, which is 28.7% for the Ra80 case. The maximum GEP-based $J(Nu)$ for all testing cases is 9.5%, which shows the significant improvement achieved by GEP training. Moreover, the performance of the models trained on each Ra is generally better than the performance for the other cases; see the diagonal component in Fig. 10(a), and interestingly, there are exceptional cases such as Ra90, where $J(Nu)$ is the largest for itself (6.7%). Nevertheless, the best model via the *frozen* approach resulting from the Ra63 case can reduce $J(Nu)$ to 3.5% for all the VNC cases. Similarly, Fig. 11(a) shows the performance of trained models with cost function $J(\overline{v\theta})$ for Θ in an *a posteriori* sense. The legend is scaled by the square root error $J(\Theta)$ of the baseline model, which is 11.5×10^{-3} for the Ra80 case. In contrast to the universal and significant improvement seen for $J(Nu)$, the error reduction on $J(\Theta)$ is relatively small across different Ra cases. The reduction of predictive error is 6.1% with respect to the maximum baseline error for Ra80 by the frozen trained models at Ra50. However, we can obtain a generalized GEP model. The best model via the *frozen* approach results from the Ra73 case, which can reduce $J(\Theta)$ to 5.6×10^{-3} for all the VNC cases, achieving approximately 50% improvement. In brief, the machine learnt models are independent of Ra for VNC cases, and the GEP models via the *frozen* approach generally perform better than baseline models, especially at the higher Ra range.

Fig. 12 illustrates the performance of GEP models trained on Ri18, R50, and Ri94 cases via *frozen* training. The baseline model perfectly captures Nu for forced convection $Ri_b = 0$. However, the prediction errors of both Nu and $\overline{v\theta}$ linearly increase with the growth of the buoyancy effect (see Fig. 12 (a), (c)). Conversely, the error reductions of GEP models trained on the Ri94 case nearly linearly increase with the decrease in the buoyancy factor. The resulting models trained on Ra50 significantly reduce the error of Nu to 5%. Moreover, all the GEP models can reduce the prediction error of $\overline{v\theta}$. Surprisingly, for the mean temperature, the baseline model is better than all the GEP modes trained on different Ri_b cases via *frozen* training except the largest Ri_b . To summarize, the GEP models depend on different Ri_b cases, where the middle range case Ri50 shows the best performance for Nu if we regard the Ri00 case as an exception. This result further suggests the limitation of the *frozen* training approach.

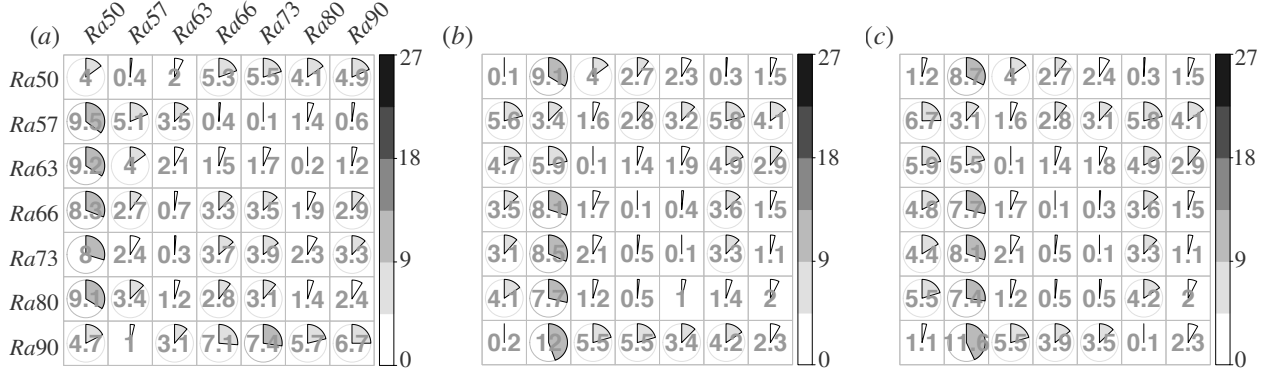


Figure 10: Error of Nu , premultiplied by 100, ($J(Nu)$ see Eq.13a) with various GEP models, (a) *ncflux*; (b) *ncnu*; (c) *ncgrad*. The row label means training a GEP model at this Ra , the column means testing the performance of a model in an *a posteriori* sense at this Ra . The color bar is based on the maximum $J(Nu)$ with baseline models, which occurs in the Ra80 case ($J(Nu) = 28.7\%$).

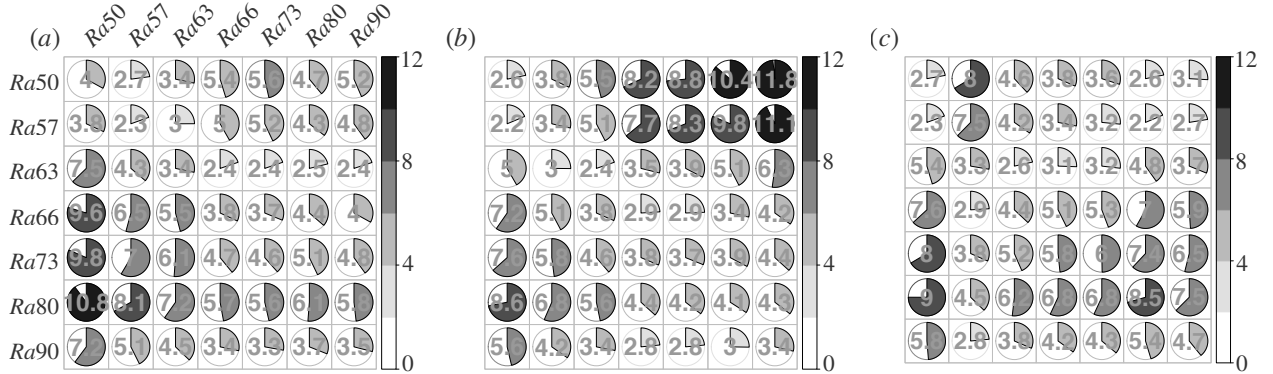


Figure 11: Error of Θ ($J(\Theta)$, premultiplied by 1000, see Eq.13a) with various GEP models, (a) *ncflux*; (b) *ncmean*; (c) *ncgrad*. The row label means training a GEP model at this Ra , the column means testing the performance of a model in an *a posteriori* sense at this Ra . The color bar is based on the maximum $J(Nu)$ with baseline models, which occurs in the Ra90 case.

4.2.2 Effects of training approaches

The comparison of training approaches is the assessment on cost functions for the data-driven method. When we select $J(Nu)$ as the cost function, i.e. we use the *CFD-driven* approach, the performance of GEP models on the prediction of Nu is generally better than that of using other cost functions. For instance, for VNC, Fig. 10(b) depicts the *a posteriori* correlation error of Nu trained by $J(Nu)$ via the *CFD-driven* approach and shows the diagonal component, which means training and testing for the same case, is smaller than that of Fig. 10(a) (trained by $J(\bar{v}\theta)$ via the *frozen* approach, i.e. without involving CFD while training). This is also true for the *a posteriori* prediction of $J(\Theta)$, when the models are trained on $J(\Theta)$ (using the *CFD-driven* approach), see Fig. 11(b), rather than when using training based on $J(\bar{v}\theta)$ via the *frozen* approach (Fig. 11(a)). Accordingly, when we select $J(Nu)$ as the cost function, it can undermine the performance on Θ of the resulting GEP models and vice versa. The maximum *a posteriori* error of $J(Nu)$ trained by cost function $J(\Theta)$ is 18.3%, which is worse than training by $J(Nu)$. However, the performance of GEP models constrained by $J(d\Theta/dy)$ (Fig. 10(c) and Fig. 11(c)) is slightly better than that of $J(\bar{v}\theta)$. Overall, the model trained on Ra73 by $J(d\Theta/dy)$ (*ncgrad* in Table 3) seems to be the best model for VNC.

For VMC, as stated in §4.2.1, the *frozen* approach can reduce the error of Nu , but the performance on Θ is even worse than when using the baseline. Fig. 13 shows the effect of various cost functions (see Table 4) based on Ra50. All the *CFD-driven*-based results can achieve a better prediction than the frozen approach for both Nu and $\bar{v}\theta$. Interestingly, the models developed with $J(\Theta)$ in the cases *mcmean* and *mccnu* (see Table 4) perform better than the frozen approach but worse than the baseline model. In contrast, they can reduce the error in Θ (see Fig. 13 (b)) at the low Ri_b regime for the cost function with the inclusion of $d\Theta/dy$ (cases *mcgrad* and *mcdc*). Moreover, when we investigate the

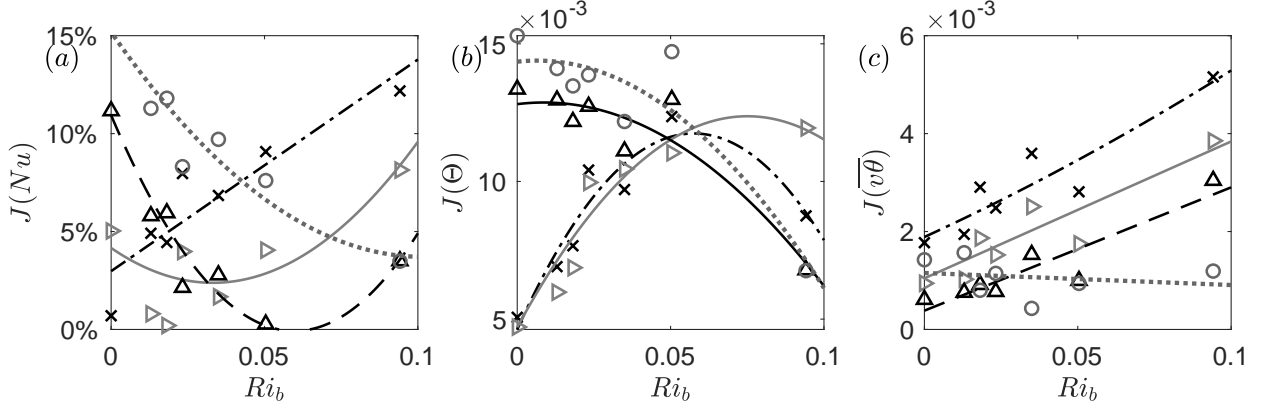


Figure 12: Error metric with the baseline or GEP models, (a) error of Nusselt number $J(Nu)$ (see Eq.13a); (b) error of mean temperature (see Eq.11 where $\varphi = \Theta$); (c) error of wall-normal heat flux (see Eq.11 where $\varphi = \overline{v\theta}$). At each Ri_b , \times , *base*; \triangleright , trained on $Ri_b = 0.018$, $f(I, J) = 1.141 + I(0.387 - 0.387J) - 0.141J$, \triangle , *mcflux*, trained on $Ri_b = 0.050$; \circ , trained on $Ri_b = 0.094$, $f(I, J) = 0.966 - I - 2(-0.43 + I)(I - 0.089J)J$, *mcgrad*. For each model, we plot a fitting curve to show the trend of error at different Ri_b , - · - ·, *base*; - - -, *mcflux*, trained on Ri_{50} ; —, trained based on Ri_{18} , - - -, trained based on Ri_{94} .

combination of quantities of interest, the *mcdc* case is the best model for the VMC cases. To summarize, the influence of training approaches for VMC cases is more significant than that for VNC cases. With the precondition of training on the middle range Ri_b case, we finally find a machine learnt model via the *CFD-driven* approach with the cost function $J(\Theta) + \lambda_2 J(d\Theta/dy)$ that performs well for all the considered Ri_b cases.

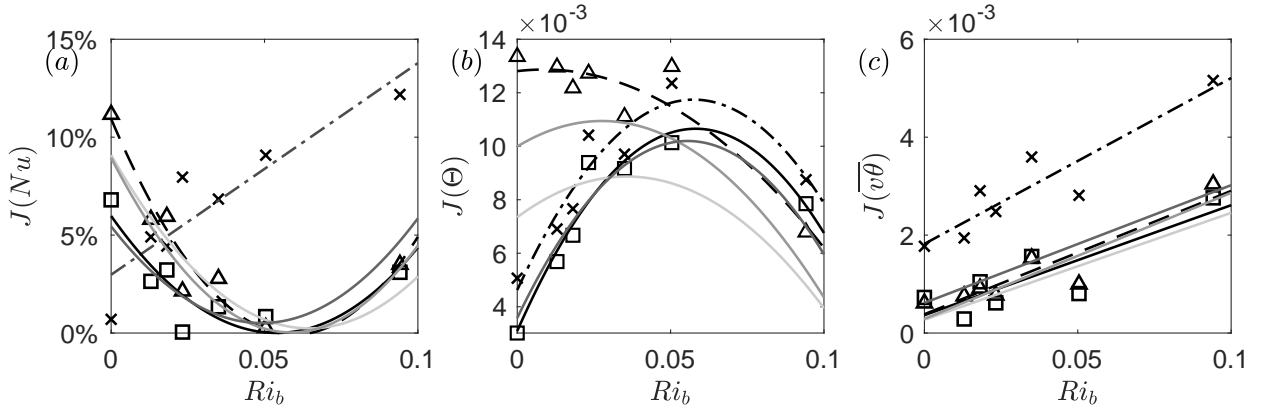


Figure 13: Error metric with baseline or GEP models, (a) error of the Nusselt number $J(Nu)$ (see Eq.13a); (b) error of the mean temperature (see Eq.11 where $\varphi = \Theta$); (c) error of wall-normal heat flux (see Eq.11 where $\varphi = \overline{v\theta}$). At each Ri_b , \times , *base*; \triangle , *mcflux*; \square , *mcgrad*. For each model, we plot a fitting curve to show the trend at different Ri_b cases, - · - ·, *base*; - - -, *mcflux*; *CFD-driven*, —, from light to heavy, *mcmean*, *ncnu*, *mcdc*, *mcgrad*, the heaviest (black) solid line, *mcgrad*.

4.3 A priori test on the turbulent Prandtl number

The predicted turbulent Prandtl number for VNC is shown in Fig. 14, where the DNS results [Ng et al., 2015] and baseline calculate with a constant $Pr_t = 0.90$ are included, with Ra spanning four decades from 10^5 to 10^9 . The Pr_t has the same feature. In the turbulent layer region ($y_2 < y_w < h$), Pr_t^{dns} remains at a constant value, which stays in the range of $0.85 \sim 1.0$ across different Ra numbers. Therefore, constant Pr_t may turn out to be a good approximation as $Ra \rightarrow \infty$ and the region of infinity anomaly diminishes. Conversely, it shows that the machine learnt model provides spatially varying Pr_t in the near-wall region. It is essential that the resulting GEP model can identify the adjustment

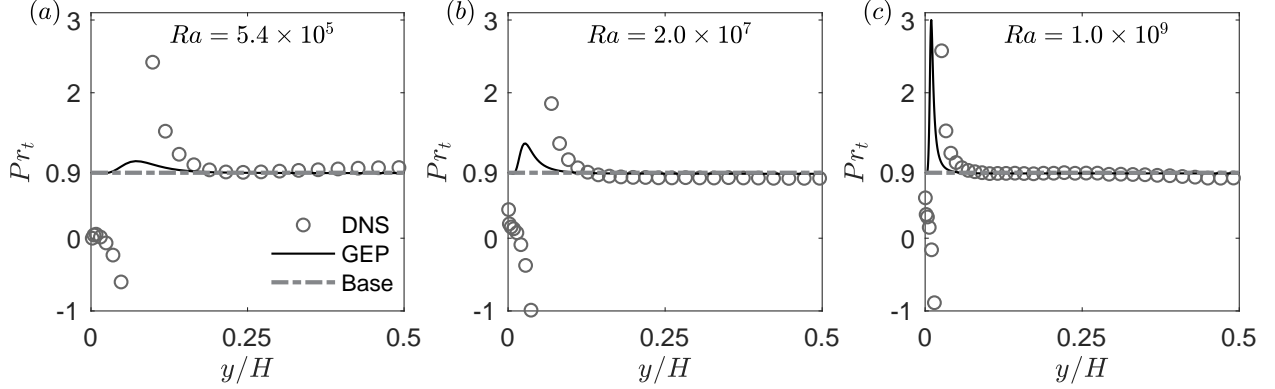


Figure 14: *A priori* test on the turbulent Prandtl number for VNC based on the resulting models trained on $Ra = 2.0 \times 10^7$.

region ($y_1 < y < y_2$) and bridge the infinity region of Pr_t with a finite value, without any user intervention, due to the self-adapting feature of dimensionless frame invariants.

In Fig. 15, the GEP generated Pr_t for VMC (Table 4, *mcgrad*) is compared against the DNS-based Pr_t [Sutherland et al., 2015] and a constant $Pr_t = 0.90$ for different Ri_b . In the very near-wall region, I and J are near zero (owing to $k = 0$ at the hotter ($y/h = 0$) and colder ($y/h = 2$) walls); hence, $Pr_t = 1/f(I, J) = 0.91$, which is smaller than the DNS near-wall results. Away from each wall, the Pr_t^{gEP} quickly reaches a maximum (at approximately 1.4) near $y^+ = 10$, while the maxima of Pr_t^{dns} (see Fig. 5) are close to each wall. However, they both decrease to 0.90 before entering the infinity region (near y_2). Moreover, the agreement between GEP and DNS results is not as good compared with VNC case. One possible reason could be the discrepancy of the approximated eddy viscosity ν_t^{mod} with DNS-based eddy viscosity. Nevertheless, the *a priori* assessment shows GEP explicitly returns a variable Pr_t , and the infinity regions are approximated by values of nearly 0.90 across the different Ri_b cases.

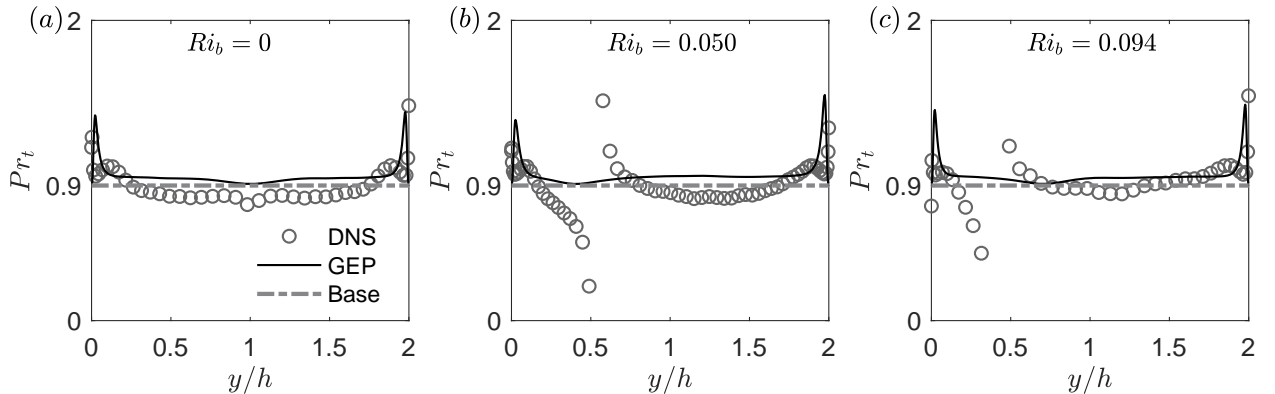


Figure 15: *A priori* test on the turbulent Prandtl number for VMC based on the models resulting from training on $Ri_b = 0.050$.

4.4 *A posteriori* performance for quantities of interest

Fig. 16(a)) shows the comparison of Nu resulting from the baseline and GEP models with DNS data at different Ra numbers. The baseline model significantly underpredicts the Nu , especially at higher Ra , with an absolute percentage error over 25%. Conversely, the GEP models can successfully predict the classical heat-transfer relationship $Nu \sim Ra^{1/3}$. Fig. 16(b) illustrates Nu versus Ri_b for VMC. Interestingly, as we showed earlier, the baseline can nearly perfectly predict Nu in the forced convection case but considerably overpredicts Nu with at least 10% absolute percentage error for higher Ri_b values. The performance of the GEP models reduces the error to less than 5%.

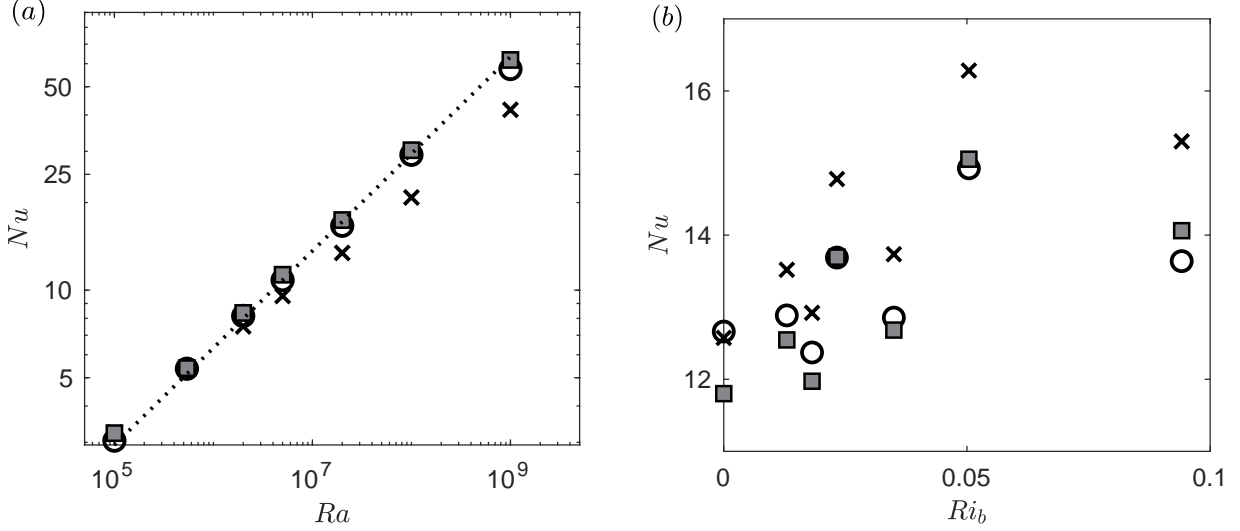


Figure 16: A *a posteriori* assessment of the Nusselt number, \circ , DNS; \blacksquare , GEP; \times , base; (a) Nu versus Ra for VNC, on a log-log scale, \dots , $Nu = 0.071(RaPr)^{1/3}$ by Versteegh and Nieuwstadt [1999]; (b) Nu versus Ri_b for VMC.

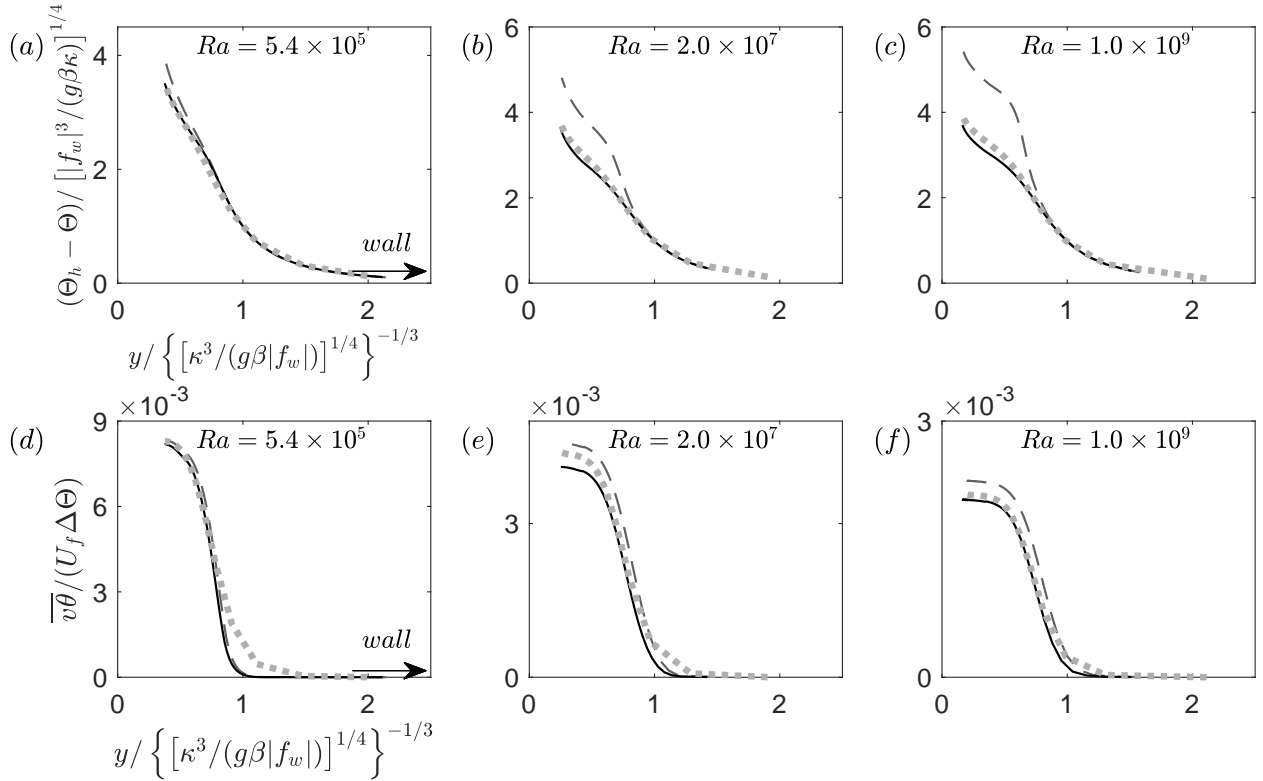


Figure 17: A *a posteriori* assessment of (a ~ c) mean temperature profile, (d ~ f) wall-normal heat flux for VNC; here, inner scaling [George Jr and Capp, 1979, Ng et al., 2013] is used. — GEP, \dots DNS, - - - baseline.

Further results for the mean profile and wall-normal heat flux are shown in Fig. 17 for VNC and Fig. 18 for VMC. In Fig. 17, (a ~ f) are plotted with an inner layer scaling [George Jr and Capp, 1979, Ng et al., 2013], where the inner temperature scales $[|f_w|^3 / (g\beta\kappa)]^{1/4}$ and the inner length scale $[\kappa^3 / (g\beta|f_w|)]^{1/4}$, in order to show the near-wall results. Due to the asymmetry profiles, here, we only show the half channel from the hotter wall. It is clear that the GEP model is better than the baseline for Θ and $\overline{v\theta}$ at the bulk region. In total, GEP-based models are fairly good, and the

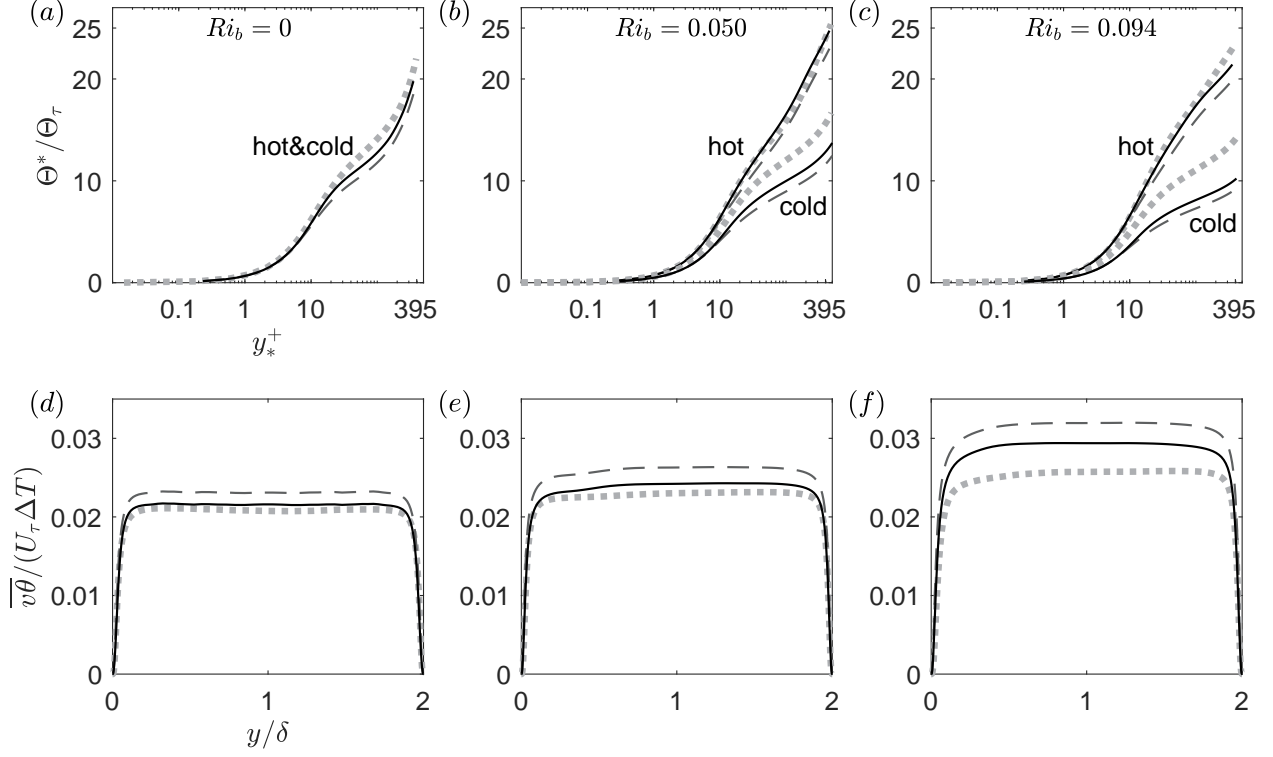


Figure 18: A posteriori assessment of (a ~ c) mean temperature profile (at the hotter wall, $\Theta^* = \Theta_c - \Theta$, $y_*^+ = y_h^+$; at the colder wall, $\Theta^* = \Theta - \Theta_c$, $y_*^+ = y_c^+$). It is normalized by $\Theta_\tau = d\Theta/dy|_w \alpha/U_\tau$, where $\alpha = 1/(Re_\tau Pr)$, and (d ~ f) wall-normal heat flux profile for VMC. — GEP, \cdots DNS, - - - baseline.

improvement holds for the whole field for VNC. Moreover, for VMC, Fig. 18(a ~ c) shows the mean temperature Θ profile along the hotter and colder wall, respectively, and Fig. 18(d ~ f) depicts the wall-normal heat flux $\overline{v\theta}$ in the global coordinates. Compared with the VNC case, the performance of baseline models is better, yet there is still room to improve. Although the baseline model correctly predicts the Nu in the forced convection case, surprisingly, the improvement of GEP models on Θ and $\overline{v\theta}$ is consistently better than the baseline at different Ri_b ($0 \leq Ri_b \leq 0.094$).

5 Concluding remarks

As the angle between the gravitation direction and temperature gradient reaches 90° , the turbulent Prandtl number Pr_t and eddy viscosity ν_t tend to infinity in a thin adjustment region between the near-wall laminar-viscosity layer and the bulk turbulent region for vertical natural convection (VNC) in a range of Rayleigh numbers ($10^5 \sim 10^9$). Whereas recent studies on VNC adopt an inner-outer two-layer structure [George Jr and Capp, 1979, Hölling and Herwig, 2005, Ng et al., 2013, 2015], we argue that this extra adjustment region can be identified by the zero point of Reynolds shear stress and the mean velocity gradient. Meanwhile, for vertical mixed convection (VMC) it also exists singular points of Pr_t and ν_t . They vary with increase of the buoyancy force, as the mean velocity maximum shift from the centreline to the hotter wall. This finding indicates that the primary effect of buoyancy on the mean profile for VMC is the break of symmetry, even for the flow in the shear-dominated regime ($0 < Ri_b < 0.1$).

To approximate the essential thermal quantities, including Nusselt number, mean temperature and wall-normal heat flux, we implement the machine learning framework via gene expression programming (GEP) to develop new turbulent heat flux models by using the DNS-based velocity fields as input for turbulent natural and mixed convection in a vertical channel. Furthermore, a sensitivity study on the training dataset and cost functions via both *frozen* and *CFD-driven* concepts are implemented to find the best prediction of the Nusselt number, mean temperature, and wall-normal heat flux. Comparing the *a posteriori* performance on Nu , Θ , and $\overline{v\theta}$, we discover that the error of the baseline (a constant $Pr_t = 0.90$) model for VNC case is larger than for the VMC case, and it is relatively easy to find effective GEP models for VNC. The data-driven method in this study is almost independent of the training dataset and cost function for the VNC case. In contrast, the VMC cases needs a strict selection of both the training dataset and cost functions. We

discover that the inclusion of the mean gradient, which acts as a bridge between first- and second-order statistics, in the cost function shows significant advantages in finding a better GEP model. This is also true for the VNC cases. In general, using cost functions that include the mean temperature gradient based on the middle range of the DNS dataset across the parameter space for both VNC and VMC can obtain a better model.

The best performing GEP models can predict Nu within a 5% absolute percentage error for the VNC case across four decades of Ra ($10^5 \sim 10^9$) and for VMC in the entire range of $0 < Rib < 0.1$ at a mean friction Reynolds number of 395, even though the training is carried out for a specific DNS dataset case. The reduction of error by GEP models is achieved across the current parameter space and cover all of the domain without any regional treatment. It is also important that the data-driven method overcomes the singularity issues of linear gradient-based models with a spatially varying Pr_t .

The RANS model development is an odyssey when the pursuit is generality and universality. Nevertheless, we can show the robustness and accuracy of the current GEP models for the turbulent Prandtl number. We capture the correct physics of the turbulent Prandtl number, but concede that the result of full RANS-based CFD for VNC and VMC would still benefit from further improvement. One avenue to pursue in future work is addressing the fact that the time and length scale calculated by k and ε (or ω) in RANS have a large discrepancy with the DNS dataset in the near-wall region, which undermines the suitability of the dimensionless velocity and temperature invariants.

Declaration of Competing Interest

We wish to confirm that there are no known conflicts of interest associated with this publication.

Acknowledgements

Xiaowei Xu was supported by the China Scholarship Council (No. 201606260057). We are indebted to Dr. Henry S. Dol, Dr. Chong Shen Ng, and Dr. Duncan Sutherland for providing the post-processed DNS data.

Appendix A, DNS on vertical mixed convection

The cited turbulent mixed convection cases are conducted by Sutherland et al. [2015]. As the reference is an abstract for the American Physical Society (APS) conference, it lacks computational details. Therefore, after private communication, we can provide the simulation setup and governing equations. As previously mentioned, some flow parameters are held constant for all simulations. $Pr = 0.709$, $\Delta\Theta = 1$, and $g_1\beta = (-1, 0, 0)$. All simulations are carried out with computational domain size $(L_x, L_y, L_z) = (16h, 2h, 8h)$. The present grid spacing is uniform in the x - and z -directions and is stretched by a non-uniform Chebyshev grid $y_j = L_y \cos(\pi j/N_y)/2$ in the y -direction to resolve the steep, near-wall gradients. The number of grid points N_x , N_y , and N_z are chosen following Kim et al. [1987], so that the $\Delta x^+ \approx 10$, $\Delta y^+ \approx 0.05$ and $\Delta z^+ \approx 5$ and to maintain an aspect ratio of approximately one in the centre of the channel. The time step is chosen to satisfy the CFL condition.

$$\frac{\partial u_i}{\partial x_i} = 0, \quad (18)$$

$$\frac{\partial u_i}{\partial t} + u_j \frac{\partial u_i}{\partial x_j} = -\frac{1}{\rho_0} \frac{\partial p}{\partial x_i} + \delta_{i1} g_1 \beta \Theta + \nu \frac{\partial^2 u_i}{\partial x_j^2}, \quad (19)$$

$$\frac{\partial \Theta}{\partial t} + u_j \frac{\partial \Theta}{\partial x_j} = \kappa \frac{\partial^2 \Theta}{\partial x_j^2}. \quad (20)$$

The numerical scheme used is a fully conservative fourth-order finite difference method on a staggered grid for the velocities following Morinishi et al. [1998], and the temperature field is advected using the QUICK scheme [Leonard, 1979]. Time-stepping is accomplished by a low-storage third-order Runge-Kutta scheme due to Spalart et al. [1991]. The continuity equation is enforced using the time-splitting method [Kim and Moin, 1985]. The solver has been successfully used for some recent studies, for example, Chung and Matheou [2012] and Ng et al. [2015].

References

Batchelor, G., 1954. Heat transfer by free convection across a closed cavity between vertical boundaries at different temperatures. *Q. Appl. Math.* 12, 209–233.

label	Flow case	Re_b	Ra	Ri_b	Re_τ^g	Re_τ^h	Re_τ^c	Nu	N_x	N_y	N_z
Ri00	Ra0_Re4.1	13846	0	0	395.33	395.37	395.28	12.75	512	256	256
Ri13	Ra6.3_Re4.2	14239	1.9×10^6	0.013	405.33	418.86	391.80	12.79	512	256	256
Ri18	Ra6.3_Re4.1	12963	2.2×10^6	0.018	375.19	391.45	358.94	12.32	512	256	256
Ri23	Ra6.5_Re4.2	14710	3.6×10^6	0.023	419.81	440.46	399.16	13.57	512	384	256
Ri35	Ra6.6_Re4.1	12696	4.0×10^6	0.035	370.92	396.04	345.79	12.86	512	384	256
Ri50	Ra6.9_Re4.2	15232	8.3×10^6	0.050	438.10	484.09	392.11	14.88	512	384	256
Ri94	Ra7.0_Re4.1	11825	9.3×10^6	0.094	356.11	398.27	313.95	13.54	512	384	256

Table 5: List of parameters for a vertical buoyant turbulent channel. $Re_b = 2hU_b/\nu$ is the bulk Reynolds number, $Re_\tau^g = hU_\tau/\nu$ is the friction Reynolds number, $Ri_b = 2\beta g\Delta\Theta h/U_b^2$ is the bulk Richardson number, $Ra = \beta g\Delta\Theta(2h)^3/(\alpha\nu)$ is the Rayleigh number, $Nu = (2h/\Delta\Theta)|d\Theta/dy|_w$ is the Nusselt number. N_x, N_y, N_z are the number of grid points in the streamwise, wall-normal, and spanwise directions, respectively. The grid is stretched using a Chebyshev grid.

- Boudjemadi, R., Maupu, V., Laurence, D., Quéré, P.L., 1997. Budgets of turbulent stresses and fluxes in a vertical slot natural convection flow at rayleigh $Ra = 10^5$ and 5.4×10^5 . *Int. J. Heat Fluid Flow* 18, 70–79.
- Chung, D., Matheou, G., 2012. Direct numerical simulation of stationary homogeneous stratified sheared turbulence. *J. Fluid Mech.* 696, 434–467.
- Dol, H., Hanjalić, K., Versteegh, T., 1999. A DNS-based thermal second-moment closure for buoyant convection at vertical walls. *J. Fluid Mech.* 391, 211–247.
- Duraisamy, K., Iaccarino, G., Xiao, H., 2019. Turbulence modeling in the age of data. *Annu. Rev. Fluid Mech.* 51, 357–377.
- Fabregat, A., Pallares, J., Vernet, A., Cuesta, I., Ferré, J., Grau, F., 2010. Identification of near-wall flow structures producing large wall transfer rates in turbulent mixed convection channel flow. *Comput. Fluids* 39, 15–24.
- Garcia-Villalba, M., del Alamo, J.C., 2011. Turbulence modification by stable stratification in channel flow. *Phys. Fluids* 23, 045104.
- George Jr, W.K., Capp, S.P., 1979. A theory for natural convection turbulent boundary layers next to heated vertical surfaces. *Int. J. Heat Mass Transfer* 22, 813–826.
- Gibson, M., Launder, B., 1978. Ground effects on pressure fluctuations in the atmospheric boundary layer. *J. Fluid Mech.* 86, 491–511.
- Gibson, M., Leslie, D., 1984. The turbulent Prandtl number in the flow near a heated vertical surface. *Int. Commun. Heat Mass Transf.* 11, 73–84.
- Hanjalić, K., 2002. One-point closure models for buoyancy-driven turbulent flows. *Annu. Rev. Fluid Mech.* 34, 321–347.
- Hölling, M., Herwig, H., 2005. Asymptotic analysis of the near-wall region of turbulent natural convection flows. *J. Fluid Mech.* 541, 383.
- Jackson, J., Cotton, M., Axcell, B., 1989. Studies of mixed convection in vertical tubes. *Int. J. Heat Fluid Flow* 10, 2–15.
- Kasagi, N., Nishimura, M., 1997. Direct numerical simulation of combined forced and natural turbulent convection in a vertical plane channel. *Int. J. Heat Fluid Flow* 18, 88–99.
- Kays, W.M., 1994. Turbulent Prandtl number, where are we? *J. Heat Transfer* 116, 284–295.
- Kim, J., Moin, P., 1985. Application of a fractional-step method to incompressible Navier-Stokes equations. *J. Comput. Phys.* 59, 308–323.
- Kim, J., Moin, P., Moser, R., 1987. Turbulence statistics in fully developed channel flow at low Reynolds number. *J. Fluid Mech.* 177, 133–166.
- Kiš, P., Herwig, H., 2014. Natural convection in a vertical plane channel: DNS results for high Grashof numbers. *Heat and Mass Transfer* 50, 957–972.
- Kutz, J.N., 2017. Deep learning in fluid dynamics. *J. Fluid Mech.* 814, 1–4.
- Leonard, B.P., 1979. A stable and accurate convective modelling procedure based on quadratic upstream interpolation. *Comput. Methods Appl. Mech. Eng.* 19, 59–98.

- Li, D., 2019. Turbulent Prandtl number in the atmospheric boundary layer-where are we now? *Atmos. Res.* 216, 86–105.
- Li, D., Katul, G.G., Zilitinkevich, S.S., 2015. Revisiting the turbulent Prandtl number in an idealized atmospheric surface layer. *J. Atmos. Sci.* 72, 2394–2410.
- Ling, J., Ryan, K.J., Bodart, J., Eaton, J.K., 2016. Analysis of turbulent scalar flux models for a discrete hole film cooling flow. *J. Turbomach.* 138, 011006.
- Mellor, G.L., Yamada, T., 1982. Development of a turbulence closure model for geophysical fluid problems. *Rev. Geophys.* 20, 851–875.
- Milani, P.M., Ling, J., Eaton, J.K., 2020. Turbulent scalar flux in inclined jets in crossflow: counter gradient transport and deep learning modelling. arXiv preprint arXiv:2001.04600 .
- Milani, P.M., Ling, J., Saez-Mischlich, G., Bodart, J., Eaton, J.K., 2018. A machine learning approach for determining the turbulent diffusivity in film cooling flows. *J. Turbomach.* 140, 021006.
- Monin, A.S., Obukhov, A.M., 1954. Basic laws of turbulent mixing in the surface layer of the atmosphere. *Contrib. Geophys. Inst. Acad. Sci. USSR* 151, e187.
- Morinishi, Y., Lund, T., Vasilyev, O., Moin, P., 1998. Fully conservative higher order finite difference schemes for incompressible flow. *J. Comput. Phys.* 143, 90–124.
- Myong, H.K., Kasagi, N., 1990. A new approach to the improvement of $k - \varepsilon$ turbulence model for wall-bounded shear flows. *JSME international journal. Ser. 2, Fluids engineering, heat transfer, power, combustion, thermophysical properties* 33, 63–72.
- Ng, C., Chung, D., Ooi, A., 2013. Turbulent natural convection scaling in a vertical channel. *Int. J. Heat Fluid Flow* 44, 554–562.
- Ng, C.S., Ooi, A., Lohse, D., Chung, D., 2015. Vertical natural convection: application of the unifying theory of thermal convection. *J. Fluid Mech.* 764, 349–361.
- Ng, C.S., Ooi, A., Lohse, D., Chung, D., 2017. Changes in the boundary-layer structure at the edge of the ultimate regime in vertical natural convection. *J. Fluid Mech.* 825, 550–572.
- Phillips, J., 1996. Direct simulations of turbulent unstratified natural convection in a vertical slot for $Pr = 0.71$. *Int. J. Heat Mass Transfer* 39, 2485–2494.
- Pirozzoli, S., Bernardini, M., Verzicco, R., Orlandi, P., 2017. Mixed convection in turbulent channels with unstable stratification. *J. Fluid Mech.* 821, 482–516.
- Reynolds, A., 1975. The prediction of turbulent Prandtl and Schmidt numbers. *Int. J. Heat Mass Transfer* 18, 1055–1069.
- Rodi, W., Mansour, N., 1993. Low reynolds number $k - \varepsilon$ modelling with the aid of direct simulation data. *J. Fluid Mech.* 250, 509–529.
- Sandberg, R., Tan, R., Weatheritt, J., Ooi, A., Haghiri, A., Michelassi, V., Laskowski, G., 2018. Applying machine learnt explicit algebraic stress and scalar flux models to a fundamental trailing edge slot. *J. Turbomach.* 140, 101008.
- Shih, T.H., Lumley, J.L., 1993. Remarks on turbulent constitutive relations. *Math. comput. model.* 18, 9–16.
- Spalart, P.R., Moser, R.D., Rogers, M.M., 1991. Spectral methods for the Navier-Stokes equations with one infinite and two periodic directions. *J. Comput. Phys.* 96, 297–324.
- Sutherland, D., Chung, D., Ooi, A., Bou-Zeid, E., 2015. The law-of-the-wall in mixed convection flow in a vertical channel. *APS* , A19–009.
- Versteegh, T., Nieuwstadt, F., 1999. A direct numerical simulation of natural convection between two infinite vertical differentially heated walls scaling laws and wall functions. *Int. J. Heat Mass Transfer* 42, 3673–3693.
- Weatheritt, J., Sandberg, R., 2016. A novel evolutionary algorithm applied to algebraic modifications of the RANS stress-strain relationship. *J. Comput. Phys.* 325, 22–37.
- Weatheritt, J., Sandberg, R., 2017. The development of algebraic stress models using a novel evolutionary algorithm. *Int. J. Heat Fluid Flow* 68, 298–318.
- Weatheritt, J., Sandberg, R.D., Ling, J., Saez, G., Bodart, J., 2017. A comparative study of contrasting machine learning frameworks applied to RANS modeling of jets in crossflow, in: *ASME Turbo Expo 2017: Turbomachinery Technical Conference and Exposition*, American Society of Mechanical Engineers. pp. V02BT41A012–V02BT41A012.
- Weatheritt, J., Zhao, Y., Sandberg, R.D., Mizukami, S., Tanimoto, K., 2020. Data-driven scalar-flux model development with application to jet in cross flow. *Int. J. Heat Fluid Flow* 147, 118931.

- Wells, A.J., Worster, M.G., 2008. A geophysical-scale model of vertical natural convection boundary layers. *J. Fluid Mech.* 609, 111.
- Wetzel, T., Wagner, C., 2019. Buoyancy-induced effects on large-scale motions in differentially heated vertical channel flows studied in direct numerical simulations. *Int. J. Heat Fluid Flow* 75, 14–26.
- Xu, W., Chen, Q., Nieuwstadt, F., 1998. A new turbulence model for near-wall natural convection. *Int. J. Heat Mass Transfer* 41, 3161–3176.
- Zhao, Y., Akolekar, H.D., Weatheritt, J., Michelassi, V., Sandberg, R.D., 2020. RANS turbulence model development using CFD-driven machine learning. *J. Comput. Phys.* 411, 109413.
- Zilitinkevich, S., Elperin, T., Kleerorin, N., Rogachevskii, I., Esau, I., 2013. A hierarchy of energy-and flux-budget (EFB) turbulence closure models for stably-stratified geophysical flows. *Bound.-Layer Meteorol.* 146, 341–373.